Circulating extracellular microRNAs in the blood promote sociability in mice

Eisuke Dohi[1,2,7,†], Ken Matoba[1, †], Phoebe A. Garcia[1, †], Jose Francis-Oliveira[1, †], Frida Anguiano[1], Takahiro Kochi[1], Jana Badrani[1], Julia See[2], Norimichi Ito[1], Rei Mitani[2], Indigo V.L. Rose[2], Eric Y. Choi[2], Takashi Imai[2], David K. Crossman[3], Mikhail V. Pletnikov[2,6], Kenneth W. Witwer[4], Minae Niwa[1,2,5], and Shin-ichi Kano[1,2,5]*

[1]Department of Psychiatry and Behavioral Neurobiology, University of Alabama at Birmingham School of Medicine, Birmingham, AL, USA

[2]Department of Psychiatry and Behavioral Sciences, Johns Hopkins University School of Medicine, Baltimore, MD, USA

[3]Department of Genetics, University of Alabama at Birmingham School of Medicine, Birmingham, AL, USA

[4]Departments of Molecular and Comparative Pathobiology and Neurology, and The Richman Family Precision Medicine Center of Excellence in Alzheimer's Disease, Johns Hopkins University School of Medicine, Baltimore, MD, USA

[5]Department of Neurobiology, University of Alabama at Birmingham School of Medicine, Birmingham, AL, USA

[6]Present address: Department of Physiology and Biophysics, Jacobs School of Medicine and Biomedical Sciences, SUNY University at Buffalo, Buffalo, NY, USA

[7]Present address: National Institute of Neuroscience, National Center of Neurology and Psychiatry, Tokyo, Japan

[†]These authors equally contribute to this work.

*Corresponding author. Email: sikano@uabmc.edu

ABSTRACT

Extracellular vesicles (EVs) are cell-derived membrane vesicles that circulate throughout the body. Accordingly, circulating EVs and their associated molecules, such as RNAs and proteins, are regarded as promising sources of molecular biomarkers for various disorders. Cell culture-derived EVs have also drawn substantial attention as possible delivery tools for therapeutic molecules. Nevertheless, the biological impact of circulating EVs on *in vivo* physiology and pathology remains elusive. Here we report that systemic exposure to blood circulating EVs from wild-type (WT) mice attenuates sociability deficits in *Rag1*$^{-/-}$ mice. Intravenously injected WT mouse blood EVs reach the brain and restore postsynaptic inhibitory signals in the *Rag1*$^{-/-}$ medial prefrontal cortex (PFC) pyramidal neurons. Mechanistically, WT EV-associated microRNAs, miR-23a-3p and miR-103-3p, reduce PKCε expression, increasing postsynaptic $GABA_A$ receptors in the mPFC pyramidal neurons. Our findings reveal a sociability-promoting effect of blood circulating EVs and associated miRNAs with therapeutic potential for sociability deficits.

INTRODUCTION

Factors circulating in the blood can influence brain function and behavior in rodents. Previous studies on brain aging demonstrates that the transfusion of young rodent blood into aged rodents restores memory function (*1, 2*); however, it is unclear whether healthy blood components ameliorate other behavioral deficits in a non-aging context. Here, we report our discovery that intravenous injections of blood circulating EVs from socially active wild-type (WT) mice attenuate sociability deficits in immunodeficient *Rag1*$^{-/-}$ mice. WT blood-derived EVs reach the brain parenchyma, interact with neurons, and modulate postsynaptic $GABA_A$ receptor signaling. Our molecular analysis has identified miR-23a-3p and miR-103-3p as critical mediators of the positive effects of WT blood EVs on sociability. We propose that the transfusion of WT blood EV-associated miRNAs has a therapeutic potential for sociability deficits.

RESULTS

WT mouse blood transfusion ameliorates sociability deficits in immunodeficient *Rag1*$^{-/-}$ mice.

Rag1$^{-/-}$ immunodeficient mice exhibited sociability deficits in the three-chamber social interaction test (**Figures 1A** and **1B**), consistent with previous reports for immunodeficient *scid* and *Rag2*$^{-/-}$ mice (*3, 4*). These mice showed no abnormalities in the olfaction test or open field exploration (**Figures S1A, S1B**). The behavioral phenotypes were due to the lack of T and B cells, as Rag1 proteins were not expressed in the brain (**Figures S1C** and **S1D**). Adoptive transfer of splenocytes or T cells from wild-type (WT) mice ameliorated the sociability deficits of *Rag1*$^{-/-}$ mice (**Figures 1C, D, S2A,** and **S2B**). Notably, the transfer of sera from WT mice also ameliorated the sociability deficits of *Rag1*$^{-/-}$ mice (**Figure 1E**). We speculated that the components of WT mouse sera mediated the effects because the sera from *Rag1*$^{-/-}$ mice did not have a similar effect. Although IFN-γ and IL-17 were shown to modulate sociability behaviors (*3, 5*), the levels of IFN-γ and IL-17 in WT mouse sera were extremely low (i.e., mostly below the detection limit of the enzyme-linked immunosorbent assay) (**Figure S2C**), suggesting that these cytokines may not necessarily mediate the effects of serum transfer. Therefore, we explored additional components in WT mouse sera that might modulate social behaviors.

T cell-dependent rescue of sociability deficits in *Rag1*$^{-/-}$ mice is associated with changes in EV-associated miRNAs in the blood.

An increasing number of studies show that cells communicate with each other via extracellular vesicles (EVs). EVs are small membrane vesicles secreted by multiple cell types in the body under both physiological and pathological conditions (*6, 7*). EVs contain various cellular components, including RNAs, proteins, lipids, and carbohydrates, and transfer these components between cells in a paracrine and endocrine manner (*6-11*). EVs are readily detected in various body fluids, including the blood. Indeed, previous studies reported that circulating EVs in the blood reached other tissues, such as the brain and liver (*12-14*). Thus, we enriched blood EVs (bEVs) from the sera of WT and *Rag1*$^{-/-}$ mice. Although the morphology, size distribution, and concentration of bEVs were comparable between WT and *Rag1*$^{-/-}$ mice (**Figures S3A-S3E**), we observed that WT T cell transfer, which attenuated sociability deficits (**Figure 1D**), significantly modified the expression of bEV-associated miRNAs in *Rag1*$^{-/-}$ mice (**Figure S4A** and **Table S1**). Notably, these miRNAs significantly overlapped with those altered in various mouse models exhibiting sociability deficits (**Figure S4B** and **Table S2**). In addition, the potential target genes of these miRNAs were enriched with genes involved in the regulation of neurons and synapses (**Figure S4C** and **Table S3-4**). These findings suggest that bEVs and bEV-associated miRNAs may affect social behaviors.

WT bEVs ameliorate sociability deficits without affecting social novelty preference deficits in *Rag1*$^{-/-}$ mice.

To examine the direct impacts of circulating EVs in the blood on social behaviors, we intravenously injected WT bEVs into *Rag1*$^{-/-}$ mice (**Figure 1F**). Although the injection did not change the numbers of peripheral T or B cells (**Figure S5**), WT bEVs ameliorated sociability deficits in *Rag1*$^{-/-}$ mice (**Figures 1G** and **S6A**). In contrast, injection of WT bEVs did not enhance sociability in WT mice (**Figure 1H**), excluding the possibility that a mere increase in circulating EVs in the blood may enhance sociability. *Rag1*$^{-/-}$ mice also showed deficits in social novelty preference in the three-chamber social interaction test (**Figure 1I**). We thus examined the effects of WT bEVs injection on social novelty preference deficits of *Rag1*$^{-/-}$ mice. Notably, WT bEVs did not ameliorate social novelty preference deficits in *Rag1*$^{-/-}$ mice (**Figures 1J** and **S6B**), indicating a selective effect of WT bEVs on sociability and its underlying neuronal

mechanisms. Social novelty preference deficits in *Rag1*$^{-/-}$ mice were also not rescued by the transfer of either WT sera, splenocytes, or T cells (**Figures S6C** and **S6D**). Thus, our findings demonstrate that WT bEVs enhance sociability, but not social novelty preference behaviors, in socially impaired mice.

WT bEVs reach the brain parenchyma and co-localize with neurons and microglia in *Rag1*$^{-/-}$ mice.

To gain insight into the underlying mechanisms of sociability rescue, we examined the distribution of chemically and genetically labeled bEVs in the brain upon systemic injections. We first labeled WT bEVs with a lipophilic dye, PKH26, and intravenously injected them into *Rag1*$^{-/-}$ mice to monitor their distribution. As early as 1 hour after injection, labeled bEVs were detected throughout the brain, including the medial prefrontal cortex (mPFC), the hippocampus, and the cerebellum (**Figures 2A** and **B**). As lipid dye labeling may be promiscuous and generate non-EV micelles (*11*), we further examined the biodistribution using bEVs collected from the mice expressing a membrane-anchored tdTomato protein (mTmG mice) (*15*). Similar to the distribution patterns of PKH26-labeled bEVs, tdTomato-positive bEVs were detected in the mPFC of *Rag1*$^{-/-}$ mice (**Figure 2C**). Among brain cell subpopulations, WT bEVs co-localized mostly with neurons and microglia (**Figures 2D-E, S7A,** and **S7B**).

Altered mPFC neuronal activities are responsible for sociability deficits in *Rag1*$^{-/-}$ mice and attenuated by WT bEVs.

The mPFC plays a crucial role in the control of sociability behaviors (*16-19*); hence we determined the involvement of the mPFC in sociability deficits and the EV-mediated rescue in *Rag1*$^{-/-}$ mice. We first examined c-Fos immunoreactivity, an indicator of neuronal activity, to determine the influence of *Rag1* deficiency on neuronal activities in the mPFC. c-Fos expression in the mPFC was increased in *Rag1*$^{-/-}$ mice, mostly in CaMKIIa^{+} excitatory neurons, compared to WT mice (**Figures 3A-C** and **S8**). To address the causal role of these increased activities of mPFC excitatory neurons in sociability deficits in *Rag1*$^{-/-}$ mice, we then conducted chemogenetic manipulations of CaMKIIa^{+} neurons in the mPFC using an inhibitory DREADD (designer receptors exclusively activated by designer drugs) receptor, hM4D(Gi) (*20*). Expression of hM4D(Gi) via adeno-associated virus (AAV) vectors [AAV-CaMKIIa-hM4D(Gi)-mCherry] in

the mPFC of *Rag1*$^{-/-}$ mice ameliorated sociability deficits in *Rag1*$^{-/-}$ mice upon the systemic injection of a DREADD agonist, clozapine *N*-oxide (CNO) (**Figure 3D** and **S9A-D**). Notably, intravenous injection of WT bEVs attenuated c-Fos immunoreactivity in the mPFC of *Rag1*$^{-/-}$ mice (**Figures 3E** and **3F**). These data suggest that WT bEVs ameliorate sociability deficits in *Rag1*$^{-/-}$ mice by targeting altered neuronal activities in the mPFC.

WT bEVs restore inhibitory postsynaptic activities in the mPFC of *Rag1*$^{-/-}$ mice.

To gain insight into the molecular and cellular mechanisms of EV-mediated modulation of mPFC neuronal activities, we first conducted RNA-seq analysis to examine the gene expression changes in the mPFC of *Rag1*$^{-/-}$ mice following intravenous injection of WT bEVs. We also compared the mPFC gene expression patterns between WT and *Rag1*$^{-/-}$ mice. We found that WT bEV injection decreased the expression of 1171 genes and increased the expression of 856 genes in the mPFC of *Rag1*$^{-/-}$ mice (**Figure S10A** and **Tables S5-8**). We also found that 2149 genes were upregulated and 2623 genes were downregulated in *Rag1*$^{-/-}$ mPFC compared to WT mPFC. By comparing these gene sets, we identified 1280 genes whose expression was altered in the *Rag1*$^{-/-}$ mPFC and restored upon WT bEV injection. These genes were functionally related to the regulation of neurons and synapses (**Figure S10B** and **Table S9**). Interestingly, this potential link had also been revealed by the analysis of bEV-associated miRNAs that were modulated by the adoptive transfer of T cells in *Rag1*$^{-/-}$ mice (**Figure S4C**). These data suggest that WT bEVs may affect synaptic activities in the *Rag1*$^{-/-}$ mPFC.

We next used brain slice electrophysiology to record synaptic activities in the mPFC. Consistent with our RNA-seq findings, we found that the amplitudes of spontaneous inhibitory postsynaptic currents (sIPSCs) were significantly reduced in *Rag1*$^{-/-}$ mice compared to WT mice (**Figures 3G and 3H**). sIPSC frequencies showed a trending decrease but were not significantly reduced in *Rag1*$^{-/-}$ mice. In contrast, no difference was found in spontaneous excitatory postsynaptic components between WT and *Rag1*$^{-/-}$ mice (**Figures S11A** and **S11B**). Notably, incubation of *Rag1*$^{-/-}$ brain slices with WT bEVs restored the levels of sIPSC amplitudes to those seen in WT brain slices (**Figures 3G** and **3H**). These findings suggest that inhibitory postsynaptic signaling in the layer V pyramidal neurons of *Rag1*$^{-/-}$ mPFC is impaired but restored by WT bEVs.

Small RNAs associated with WT bEVs restore sociability in *Rag1*$^{-/-}$ mice.

miRNAs associated with EVs have been shown to mediate intercellular communications even across distant organs (*8, 13*). Thus, we tested if WT bEVs modulate sociability and neuronal activities via miRNAs. We extracted small RNA fractions from WT bEVs and loaded them into *Rag1*$^{-/-}$ bEVs as previously described (*21*). These *Rag1*$^{-/-}$ bEVs containing WT bEV-derived RNA (*Rag1*$^{-/-}$ bEVs + WT RNA) were intravenously injected into *Rag1*$^{-/-}$ mice and their effects on sociability were compared with those of the *Rag1*$^{-/-}$ bEVs containing *Rag1*$^{-/-}$ bEV-derived RNA (*Rag1*$^{-/-}$ bEVs + *Rag1*$^{-/-}$ RNA, negative control) and WT bEVs containing WT bEV-derived RNA (WT bEVs + WT RNA, positive control). Compared with the "*Rag1*$^{-/-}$ bEVs + *Rag1*$^{-/-}$ RNA" group, "*Rag1*$^{-/-}$ bEVs + WT RNA" group showed increased sociability, similar to the level of "WT bEVs + WT-RNA" group (**Figures S12A** and **S12B**). These findings show that small RNAs associated with WT bEVs enhance sociability in *Rag1*$^{-/-}$ mice.

Combined analysis of PFC RNA-seq and bEV miRNA-seq identifies PKCε as a target of WT bEV-associated miRNAs.

To identify the miRNA cargos by which blood EVs enhance sociability and modulate mPFC neuronal activities, we further analyzed our bEV-associated miRNA-seq data (**Figures S4A-C** and **Table S1**) and PFC RNA-seq data (**Figures S10A, S10B,** and **Tables S5-8**) to determine the potential candidate pairs of bEV-associated miRNAs and their target mRNAs (**Figure 4A**). We examined the list of 755 mRNAs whose expression in the PFC was higher in *Rag1*$^{-/-}$ mice than in WT mice and reduced by WT bEV injections (**Figure 4A** and **Table S10**). These mRNAs were the candidate targets of bEV-miRNAs whose expression decreased in *Rag1*$^{-/-}$ mice. Since WT bEVs enhanced inhibitory postsynaptic activities in the mPFC of *Rag1*$^{-/-}$ mice (**Figure 3H**), we searched for the mRNAs whose expression may impact GABAergic synapse components and found seven relevant mRNAs (**Figure 4A**). We further compared these mRNAs with the extended list of putative mRNA targets of the 40 bEV-associated miRNAs whose expression is recovered by T cell transfer in *Rag1*$^{-/-}$ mice (**Figure S4A** and **Table S11**). We then focused on the mRNAs whose overexpression reduces sIPSC amplitudes. This analysis identified *Prkce*, which encodes the PKCε protein, as a plausible target. PKCε was previously shown to reduce GABA-mediated postsynaptic inhibitory currents via downregulation of postsynaptic $GABA_A$ receptors in mice (*22*). We indeed found increased expression of PKCε at the protein level in the

Rag1$^{-/-}$ mPFC by immunohistochemistry (**Figures 4B** and **4C**). A previous study reported that PKCε decreased synaptic $GABA_A$ receptors (*22*). Indeed, we observed that amount of synaptic $GABA_A$ receptors [$GABA_A$ receptor subunit ($GABA_A$Rγ2) associated with Gephyrin] per CaMKIIα$^+$ neurons decreased in the *Rag1*$^{-/-}$ mPFC (**Figures 4D** and **4E**), which explained the reduced sIPSC amplitudes (**Figure 3G** and **3H**). Moreover, *Rag1*$^{-/-}$ bEVs were associated with significantly lower amounts of miRNAs predicted to target PKCε, miR-23a-3p and miR-103-3p (**Figure S13**), than WT bEVs (**Figure 4F**). The expression levels of miR-23a-3p and miR-103-3p in WT bEVs did not decrease by RNase treatment in the absence of detergent (**Figures S14A** and **S14B**), consistent with the previous observations that EV-associated miRNAs are protected from RNase-dependent degradation unless EVs are disrupted by detergent (*23, 24*). These findings suggest that WT bEV-associated miR-23a-3p and miR-103-3p influence the mPFC neuronal activities by modulating PKCε expression, synaptic $GABA_A$ receptor expression, and sIPSCs.

WT bEV-associated miR-23a-3p and miR-103-3p restore the mPFC neuronal activities and attenuate sociability deficits in *Rag1*$^{-/-}$ mice.

We next tested if miR-23a-3p and miR-103-3p could correct the mPFC neuronal alterations and attenuate sociability deficits in *Rag1*$^{-/-}$ mice. We loaded *Rag1*$^{-/-}$ bEVs with miRNA mimics of miR-23a-3p and miR-103-3p, and intravenously injected them into *Rag1*$^{-/-}$ mice. Then, we assessed their effects on sociability in *Rag1*$^{-/-}$ mice (**Figure 5A**). We found that *Rag1*$^{-/-}$ bEVs loaded with miR-23a-3p and miR-103-3p mimics significantly attenuated sociability deficits compared to *Rag1*$^{-/-}$ bEVs loaded with non-targeting mimics (**Figure 5B**). Attenuated sociability deficits were accompanied by reduced expression of neuronal c-Fos and PKCε in the mPFC (**Figures 5C-F**). Injections of *Rag1*$^{-/-}$ bEVs loaded with miR-23a-3p and miR-103-3p also increased the co-localization of $GABA_A$ receptor subunit ($GABA_A$Rγ2) to Gephyrin (**Figures 5G** and **5H**), suggesting that miR-103-3p and miR-23a-3p disinhibit PKCε-dependent downregulation of synaptic $GABA_A$ receptors (*22*). We also examined the effects of miR-23a-3p and miR-103-3p on synaptic activities of layer V pyramidal neurons in the mPFC of *Rag1*$^{-/-}$ mice using brain slice electrophysiology. *Rag1*$^{-/-}$ bEVs loaded with miR-23a-3p and miR-103-3p significantly enhanced the levels of sIPSCs, reminiscent of those observed by WT bEV treatment, while *Rag1*$^{-/-}$ bEVs loaded with non-targeting miRNA mimic controls had no effects

on sIPSCs (**Figures 5I** and **5J**). These findings support that bEV-associated miR-23a-3p and miR-103-3p increase inhibitory postsynaptic signaling by reducing PKCε-dependent $GABA_A$ receptor internalization (**Figure S15**) and promote sociability.

DISCUSSION

This study reveals a novel concept that blood circulating EVs and EV-associated miRNAs from socially active mice attenuate sociability impairment in mice. Our focus on immunodeficient *Rag1*$^{-/-}$ mice has led us to discover that circulating EVs enter the brain parenchyma and co-localize with neurons and microglia in the mPFC. At the molecular level, miR-23a-3p and miR-103-3p, two miRNAs enriched in socially active WT bEVs and diminished in socially impaired *Rag1*$^{-/-}$ bEVs, restore postsynaptic inhibitory signaling on layer V pyramidal neurons in the mPFC of *Rag1*$^{-/-}$ mice by reducing the expression of their common target, PKCε, and increasing synaptic localization of $GABA_AR\gamma2$. Thus, our data provide a mechanistic insight into how miRNAs associated with circulating blood EVs influence sociability behaviors and suggest that EVs and miRNAs have therapeutic potential for the treatment of sociability deficits.

PKCε was previously shown to downregulate synaptic $GABA_A$ receptors via the N-ethylmaleimide-sensitive factor and reduce the amplitudes of postsynaptic inhibitory currents in the hippocampus (*22*). Our study demonstrated that PKCε-dependent modulation of postsynaptic GABA signaling is also critical for proper synaptic function in the mPFC, the dysregulation of which leads to hyperexcitability and sociability deficits. Our data further revealed that this modulation of postsynaptic activities on pyramidal neurons was regulated by EV-associated miRNAs, miR-23a-3p and miR-103-3p, from the circulation. Local protein translation was known to control the expression of $GABA_A$ receptors and some PKC isoforms (*25-27*). In addition, miRNAs were shown to regulate $GABA_A$ receptor expression locally at dendrites (*25*). Although further mechanistic studies are required, EV-associated miR-23a-3p and miR-103-3p may directly impact the local translation of PKCε at dendrites and synapses.

Our data show that blood EV transfer from socially active mice did not improve social novelty preference in *Rag1*$^{-/-}$ mice, despite improving their sociability. Notably, the transfer of WT sera, splenocytes, and T cells also failed to improve social novelty preference, even though they

improved sociability in *Rag1*$^{-/-}$ mice. Thus, the social novelty preference deficits in *Rag1*$^{-/-}$ mice may be caused by yet-unknown mechanisms. The differential contribution of adaptive immune cells to sociability and social novelty preference needs further investigation.

Previous studies reported the altered expression of miR-23a-3p and miR-103-3p in the body fluids of patients with autism spectrum disorders (ASD) and schizophrenia (*28, 29*), typical disorders accompanied by sociability deficits. Levels of miR-23a-3p were decreased in patients with schizophrenia but increased in ASD patients. In addition, miR-103-3p showed a decrease across multiple studies with ASD patients. Consistent with our findings, one of these human studies also found that the predicted mRNA targets of miR-23a-3p were related to synaptic functions and ASD risk genes (*28*). Nevertheless, the impact of miR-23a-3p and miR-103-3p expression changes on social behaviors in patients remains unclear. Future studies will determine the association of blood miR-23a-3p and miR-103-3p expression levels with sociability and other cognitive functions in human individuals, which can contribute to a better understanding of blood-brain communication changes underlying ASD and schizophrenia.

Alterations of circulating EVs and their associated molecular cargos are detected in various brain disorders, such as psychiatric disorders and neurodegenerative diseases (*30, 31*). While blood EV alterations are useful as biomarkers, our research indicates that they may also play a crucial role in disease mechanisms involving periphery-brain communication. Importantly, our data demonstrated that the supplementation of EVs and miRNAs could improve sociability**.** Therefore, supplementing specific circulating EVs and their molecular cargos, in addition to targeting and inhibiting them, may be a promising strategy to modulate neuronal function and behaviors under physiological and pathological conditions.

Figure 1

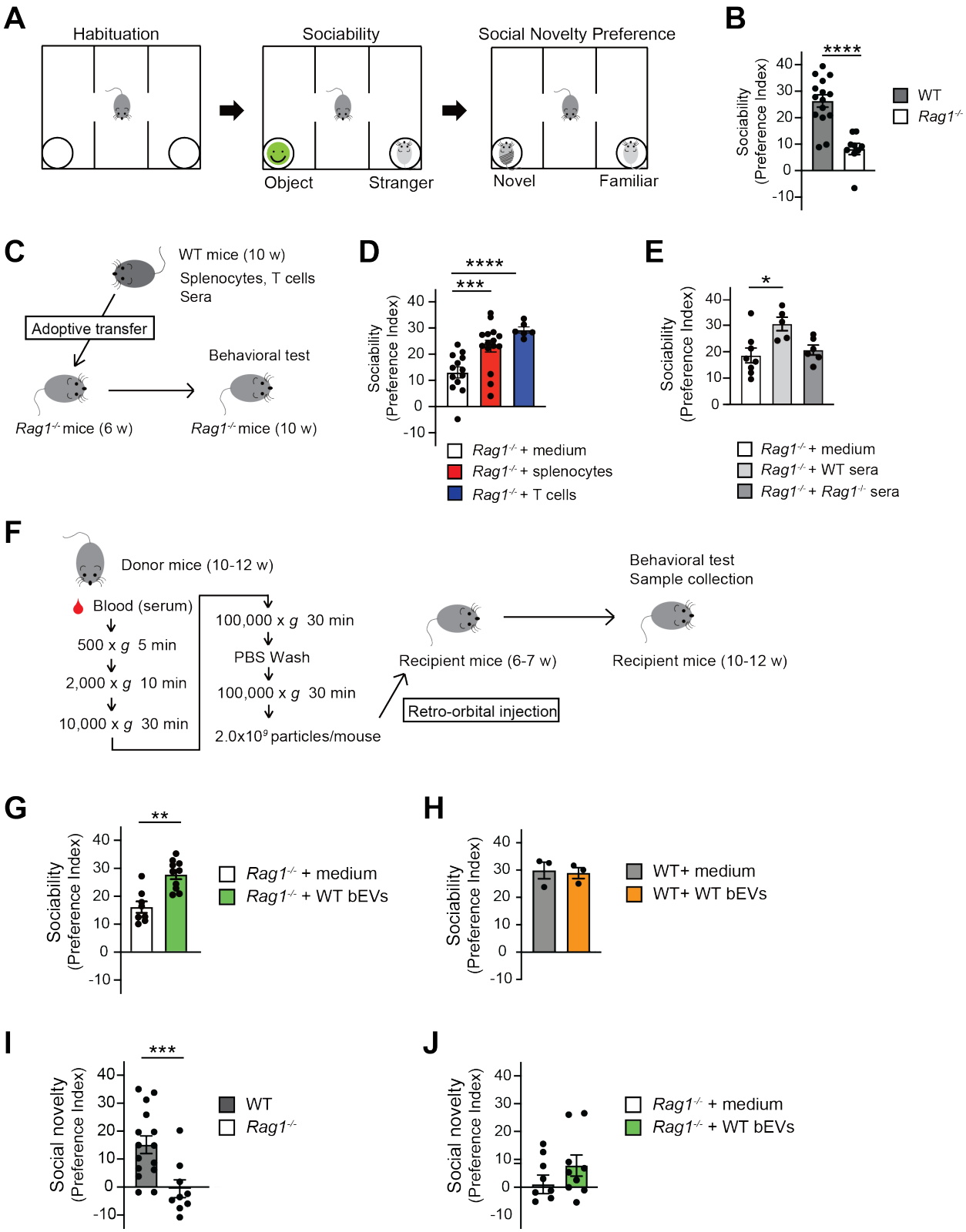
A
Habituation
Sociability
Social Novelty Preference
Object
Stranger
Novel
Familiar
B
****
Sociability (Preference Index)
WT
Rag1-/-
C
WT mice (10 w)
Splenocytes, T cells
Sera
Adoptive transfer
Behavioral test
Rag1-/- mice (6 w)
Rag1-/- mice (10 w)
D
****
***
Sociability (Preference Index)
Rag1-/- + medium
Rag1-/- + splenocytes
Rag1-/- + T cells
E
*
Sociability (Preference Index)
Rag1-/- + medium
Rag1-/- + WT sera
Rag1-/- + Rag1-/- sera
F
Donor mice (10-12 w)
Blood (serum)
500 x g 5 min
2,000 x g 10 min
10,000 x g 30 min
100,000 x g 30 min
PBS Wash
100,000 x g 30 min
2.0x10^9 particles/mouse
Retro-orbital injection
Recipient mice (6-7 w)
Behavioral test
Sample collection
Recipient mice (10-12 w)
G
**
Sociability (Preference Index)
Rag1-/- + medium
Rag1-/- + WT bEVs
H
Sociability (Preference Index)
WT+ medium
WT+ WT bEVs
I
***
Social novelty (Preference Index)
WT
Rag1-/-
J
Social novelty (Preference Index)
Rag1-/- + medium
Rag1-/- + WT bEVs

Figure 1: WT bEVs attenuate sociability deficits in *Rag1*$^{-/-}$ mice. A, Outline of the three-chamber social behavior test. **B**, Sociability in the three-chamber social interaction test by WT and *Rag1*$^{-/-}$ mice. WT mice, n = 15; *Rag1*$^{-/-}$ mice, n = 9. **C**, Experimental outline of adoptive transfer/serum injection and subsequent behavioral assay. **D,** Adoptive transfer of WT mouse splenocytes or T cells into *Rag1*$^{-/-}$ mice ameliorated their sociability deficits. *Rag1*$^{-/-}$ mice + medium, n = 13; *Rag1*$^{-/-}$ mice + WT splenocytes, n = 15; and *Rag1*$^{-/-}$ mice + WT T cells, n = 6. **E**, Intravenous injection of sera from WT mice, but not from *Rag1*$^{-/-}$ mice, into *Rag1*$^{-/-}$ mice ameliorated their sociability deficits. *Rag1*$^{-/-}$ mice + medium, n = 8; *Rag1*$^{-/-}$ mice + WT sera, n = 5; and *Rag1*$^{-/-}$ mice + *Rag1*$^{-/-}$ sera, n = 6. **F,** Experimental outline of bEV collection, intravenous injection, and subsequent behavioral assay. **G,** Intravenous injection of WT bEVs into *Rag1*$^{-/-}$ mice ameliorated their sociability deficits. *Rag1*$^{-/-}$ mice + medium, n = 8; *Rag1*$^{-/-}$ mice + WT bEVs, n = 10. **H,** Intravenous injection of WT bEVs did not enhance sociability in WT mice. WT mice + medium, n = 3; and WT mice + WT bEVs, n = 3. **I,** *Rag1*$^{-/-}$ mice also showed a reduced preference in interacting with a novel mouse versus a familiar mouse (social novel preference deficits) in the three-chamber social interaction test. WT mice, n = 15; and *Rag1*$^{-/-}$ mice, n = 9. **J,** Intravenous injection of WT bEVs did not restore social novelty preference in *Rag1*$^{-/-}$ mice. *Rag1*$^{-/-}$ mice + medium, n = 8; *Rag1*$^{-/-}$ mice + WT bEVs, n = 9. Each bar in the graphs represents mean ± SE. ns, not significant. **p*<0.05, ***p*<0.01, ****p* <0.005, *****p*<0.001. Significance was determined by Student's *t* test and one-way ANOVA with *post hoc* Dunnett's test. See Table S12 for the detail of statistical analysis.

Figure 2

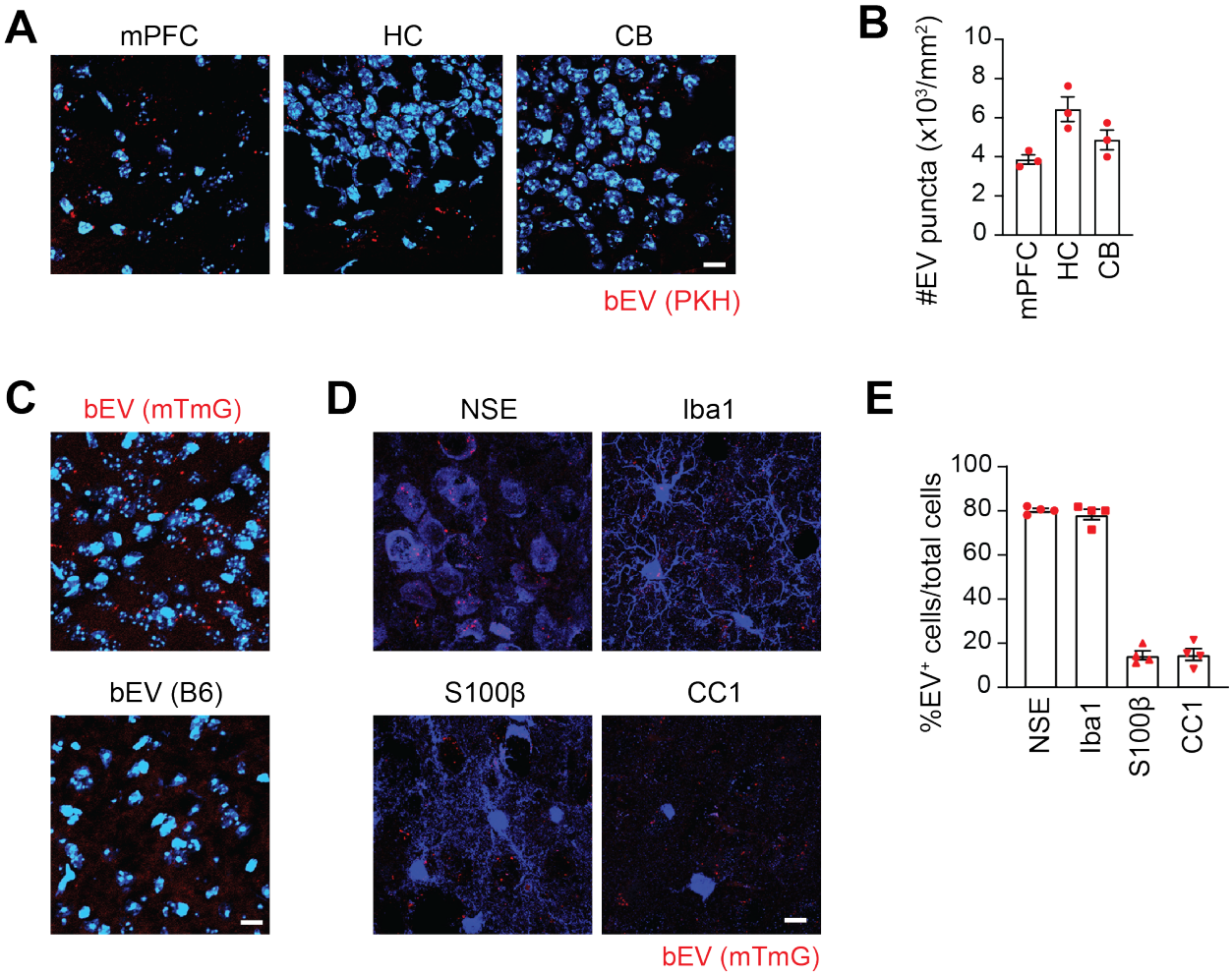
A
mPFC
HC
CB
bEV (PKH)
B
#EV puncta (x10³/mm²)
10
8
6
4
2
0
mPFC
HC
CB
C
bEV (mTmG)
bEV (B6)
D
NSE
Iba1
S100β
CC1
bEV (mTmG)
E
%EV⁺ cells/total cells
100
80
60
40
20
0
NSE
Iba1
S100β
CC1

Figure 2: WT bEVs co-localize neurons and microglia in *Rag1*$^{-/-}$ mouse brains. A, Representative confocal microscope images showing the distribution patterns of intravenously injected PKH26-labeled bEVs (Red) in the mPFC, hippocampus (HC) and cerebellum (CB) of *Rag1*$^{-/-}$ mice. DAPI stain (blue). **B,** Quantification of PKH26- labeled bEVs in the brains of *Rag1*$^{-/-}$ mice (n = 3). **C,** Representative confocal microscope images showing the distribution patterns of intravenously injected tdTomato^{+} bEVs (Red) from mTmG mice in the mPFC of *Rag1*$^{-/-}$ mice. DAPI stain (blue). **D,** Representative confocal microscope images showing the localization of tdTomato^{+} bEVs with neurons (NSE^{+} cells) and microglia (Iba1^{+} cells) in the mPFC of *Rag1*$^{-/-}$ mice. **E,** Quantification of tdTomato^{+} bEVs localized with neurons (NSE^{+} cells), microglia (Iba1^{+} cells), astrocytes (S100β^{+} cells), and oligodendrocytes (CC1^{+} cells) in the mPFC of *Rag1*$^{-/-}$ mice (n = 4). Scale bar, 10 µm. Each bar in the graphs represents mean ± SE.

Figure 3

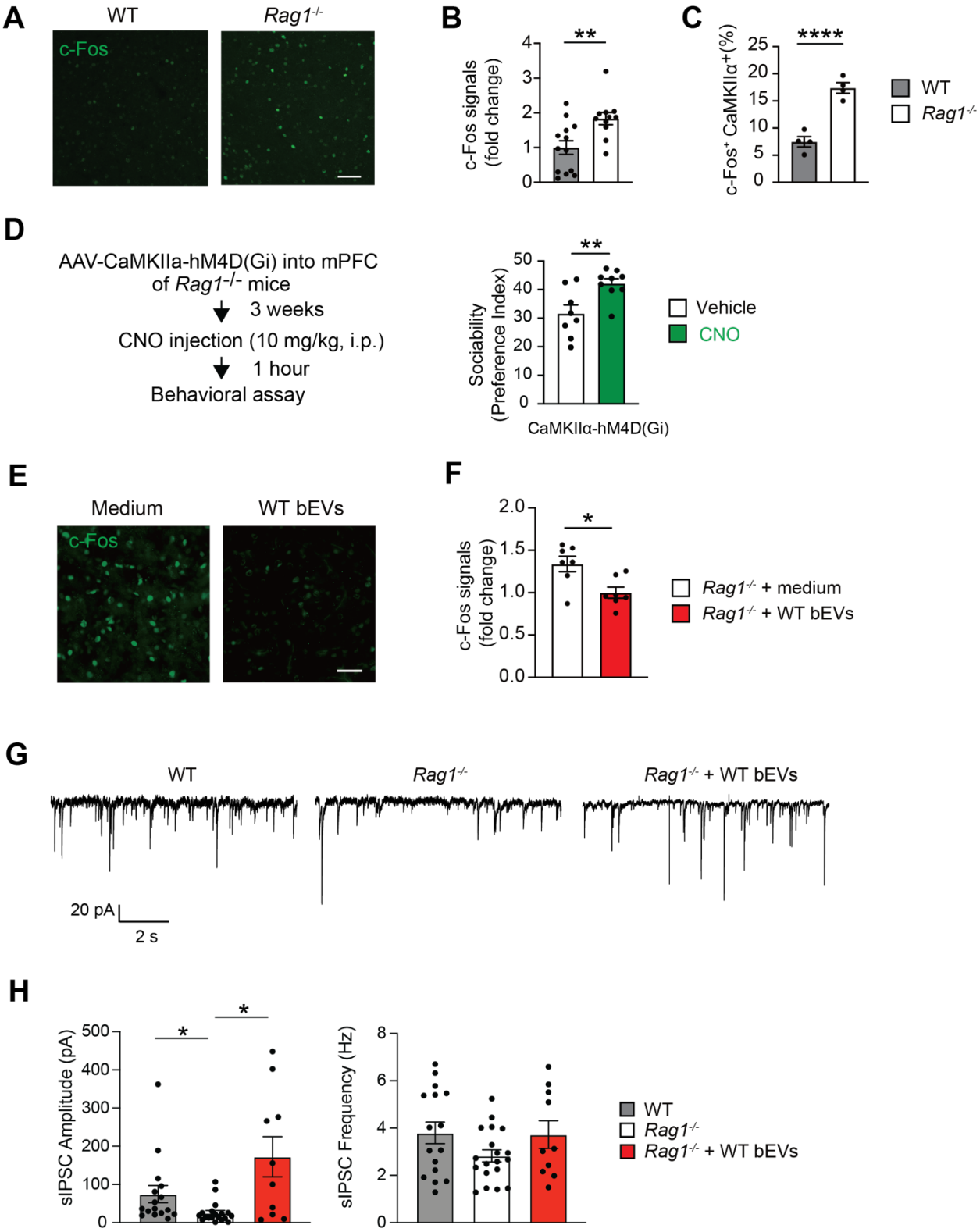
A
WT
Rag1-/-
c-Fos
B
c-Fos signals (fold change)
**
C
c-Fos+ CaMKIIα+(%)
****
WT
Rag1-/-
D
AAV-CaMKIIa-hM4D(Gi) into mPFC of Rag1-/- mice
3 weeks
CNO injection (10 mg/kg, i.p.)
1 hour
Behavioral assay
Sociability (Preference Index)
**
Vehicle
CNO
CaMKIIα-hM4D(Gi)
E
Medium
WT bEVs
c-Fos
F
c-Fos signals (fold change)
*
Rag1-/- + medium
Rag1-/- + WT bEVs
G
WT
Rag1-/-
Rag1-/- + WT bEVs
20 pA
2 s
H
sIPSC Amplitude (pA)
*
*
sIPSC Frequency (Hz)
WT
Rag1-/-
Rag1-/- + WT bEVs

Figure 3: mPFC hyperexcitability underlies sociability deficits by *Rag1*$^{-/-}$ mice and is attenuated by WT bEVs. A, Representative confocal microscope images showing an enhanced c-Fos immunoreactivity in the mPFC of *Rag1*$^{-/-}$ mice. Scale bar, 50 µm. **B,** Quantification of c-Fos-positive neurons as fold change of percentages for c-Fos^{+} cells per NeuN^{+} cells. WT mice, n = 13 *Rag1*$^{-/-}$ mice, n = 11. **C,** Quantification of c-Fos-positive CaMKIIα^{+} neurons as percentages for c-Fos cells per CaMKIIα^{+} neurons. WT mice, n = 4 *Rag1*$^{-/-}$ mice, n = 4. **D,** Chemogenetic inhibition of CamKIIα^{+} neuronal activities in the mPFC by hM4D(Gi) upon CNO injection ameliorated sociability deficits in *Rag1*$^{-/-}$ mice. Vehicle n = 8 mice; CNO n = 9 mice. **E,** Representative confocal microscope images showed a reduction of c-Fos immunoreactivity in the mPFC of *Rag1*$^{-/-}$ mice after WT bEV injection. **F,** Quantification of c-Fos-positive neurons as fold-change of percentages for c-Fos^{+} cells per NeuN^{+} cells. *Rag1*$^{-/-}$ mice + medium, n = 7; *Rag1*$^{-/-}$ mice + WT bEVs, n = 7. Scale bar, 50 µm. **G**, Representative traces of spontaneous inhibitory postsynaptic currents (sIPSC). Voltage was clamped at -70 mV, and recordings were taken for 5 min. AP-V (50 µM) and DNQX (50 µM) were added to the bath to inhibit NMDA and AMPA receptors throughout the experiment. The temperature was set at 30 ± 1°C. **H,** Quantification of sIPSC amplitude and frequency between groups. For sIPSC quantification, significance was determined by one-way ANOVA with Bonferroni correction. At least 3 different 8-10-week-old mice were used for each group. Each bar in the graphs represents mean ± SE. ns, not significant. $^{*}p<0.05$, $^{**}p<0.01$, $^{***}p<0.005$, $^{****}p<0.001$. Significance was determined by Student's *t*-test, except in **H**. See Table S12 for the details of the statistical analysis

Figure 4

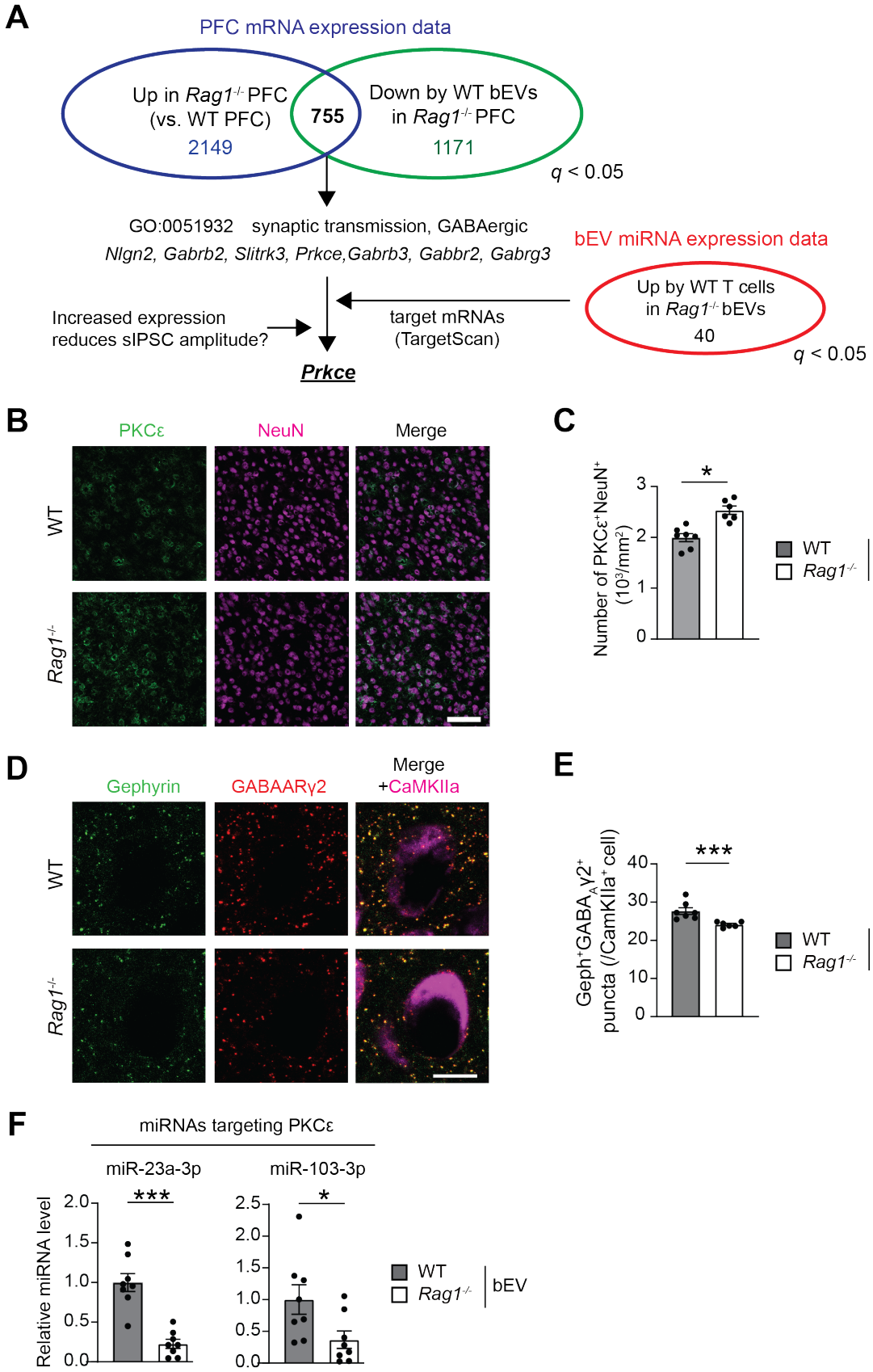
A
PFC mRNA expression data
Up in Rag1-/- PFC (vs. WT PFC)
2149
755
Down by WT bEVs in Rag1-/- PFC
1171
q < 0.05
GO:0051932 synaptic transmission, GABAergic
Nlgn2, Gabrb2, Slitrk3, Prkce, Gabrb3, Gabbr2, Gabrg3
bEV miRNA expression data
Up by WT T cells in Rag1-/- bEVs
40
q < 0.05
Increased expression reduces sIPSC amplitude?
target mRNAs (TargetScan)
Prkce
B
PKCε
NeuN
Merge
WT
Rag1-/-
C
Number of PKCε+NeuN+ (10³/mm²)
*
WT
Rag1-/-
mPFC
D
Gephyrin
GABAARγ2
Merge +CaMKIIa
WT
Rag1-/-
E
Geph+GABAAγ2+ puncta (/CamKIIa+ cell)
***
WT
Rag1-/-
mPFC
F
miRNAs targeting PKCε
miR-23a-3p
miR-103-3p
Relative miRNA level
***
*
WT
Rag1-/-
bEV

Figure 4: Combined analysis of PFC RNA-seq and bEV miRNA-seq identifies PKCε as a target of WT bEV-associated miRNAs.

A, Flow of data analysis to identify candidate genes responsible for GABAergic signaling changes in *Rag1*$^{-/-}$ mPFC. **B,** Representative confocal microscope images showing an enhanced neuronal PKCε immunoreactivity the mPFC of *Rag1*$^{-/-}$ mice. **C,** Quantification of PKCε^{+} neurons in the mPFC of WT and *Rag1*$^{-/-}$ mice (n = 7 per group). **D,** Representative confocal microscope images of neuronal Gephyrin and GABA-A expression in CaMKIIα^{+} cells in the mPFC of WT and *Rag1*$^{-/-}$ mice. **E,** Quantification of number of Gephyrin and GABA-A puncta in CaMKIIα^{+} in the mPFC of WT and *Rag1*$^{-/-}$ mice (n = 7 per group). **F,** Expression of miR-23a-3p and miR-103-3p in the bEVs from WT and *Rag1*$^{-/-}$ mice (n = 8 per group). Data are shown as fold-change relative to WT data. Scale bar, 50 µm. Each bar in the graphs represents mean ± SE. ns, not significant. $^{**}p < 0.01$, $^{***}p < 0.005$. Significance was determined by Student's *t*-test. See Table S12 for the detail of statistical analysis.

Figure 5

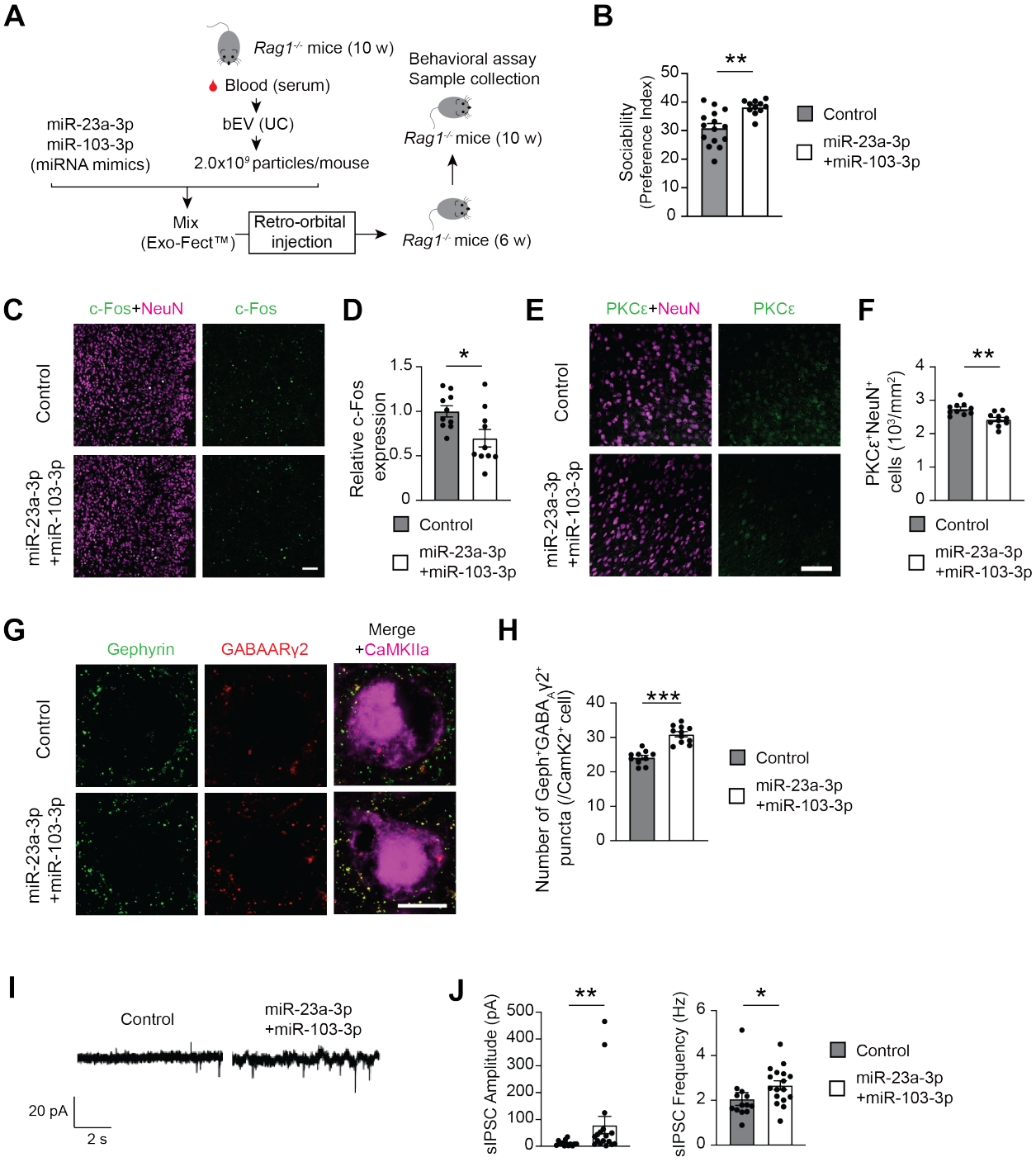
A
Rag1-/- mice (10 w)
Blood (serum)
bEV (UC)
2.0x10^9 particles/mouse
miR-23a-3p
miR-103-3p
(miRNA mimics)
Mix
(Exo-Fect™)
Retro-orbital injection
Behavioral assay
Sample collection
Rag1-/- mice (10 w)
Rag1-/- mice (6 w)
B
Sociability (Preference Index)
Control
miR-23a-3p +miR-103-3p
C
c-Fos+NeuN
c-Fos
Control
miR-23a-3p +miR-103-3p
D
Relative c-Fos expression
E
PKCε+NeuN
PKCε
F
PKCε+NeuN+ cells (10³/mm²)
G
Gephyrin
GABAARγ2
Merge +CaMKIIa
H
Number of Geph+GABAAγ2+ puncta (/CamK2+ cell)
I
Control
miR-23a-3p +miR-103-3p
20 pA
2 s
J
sIPSC Amplitude (pA)
sIPSC Frequency (Hz)

Figure 5: WT bEV-associated miR-23a-3p and miR-103-3p restore mPFC excitatory-inhibitory balance and promote sociability. A, Experimental outline of bEV collection, miRNA mimics loading, intravenous injection, and subsequent behavioral assay. **B,** Sociability data of *Rag1*$^{-/-}$ mice administered with negative control miRNA mimics (control mimics) and miRNA mimics for miR-23a-3p and miR-103-3p (miR-23a-3p + miR-103-3p mimics). Control, n = 15; miR-23a-3p + miR-103-3p, n = 11. **C,** Representative confocal microscope images of neuronal c-Fos expression in the mPFC of *Rag1*$^{-/-}$ mice administered with control and miR-23a-3p + miR-103-3p mimics (n = 10 mice per group). **D,** Quantification of c-Fos^{+} neurons in the mPFC of WT and *Rag1*$^{-/-}$ mice (n = 7 per group). **E,** Representative confocal microscope images of neuronal PKCε expression in the mPFC of *Rag1*$^{-/-}$ mice administered with control and miR-23a-3p + miR-103-3p mimics (n = 10 mice per group). **F,** Quantification of PKCε^{+} neurons in the mPFC of WT and *Rag1*$^{-/-}$ mice (n = 10 per group). **G,** Representative confocal microscope images of neuronal Gephyrin and GABA-A expression in CaMKIIα^{+} cells in the mPFC of *Rag1*$^{-/-}$ mice administered with control and miR-23a-3p + miR-103-3p mimics. **H,** Quantification of number of Gephyrin and GABA-A puncta in CaMKIIα^{+} in the mPFC of WT and *Rag1*$^{-/-}$ mice (n = 10 per group). **I,** Representative traces of sIPSCs of the mPFC layer V neurons in brain slices from *Rag1*$^{-/-}$ mice administered with control and miR-23a-3p + miR-103-3p mimics. **J,** Quantification data of sIPSC amplitude and frequency changes by miR-23a-3p + miR-103-3p mimics in *Rag1*$^{-/-}$ mice (aggregated data from n = 3 mice per group). Scale bars, 50 μm (**c** and **e**) and 10 μm (**i**). Each bar in the graphs represents mean ± SE. ns, not significant. **p*<0.05, ***p* <0.01, and ****p*<0.005. Significance was determined by Student's *t*-test. See Table S12 for the detail of statistical analysis.

Materials and Methods

Mice

Rag1$^{-/-}$ and mTmG mice (Stock# 002216 and 007676, backcrossed to C57BL/6J background), and C57BL/6J mice were purchased from the Jackson Laboratory and housed in specific pathogen-free facilities at the Johns Hopkins University and the University of Alabama at Birmingham. Male mice were used for the experiments at 8–12 weeks of age unless stated otherwise. All experimental procedures were performed under the animal protocols approved by the Institutional Animal Care and Use Committees.

Behavioral assays

Behavioral assays were performed on male mice at 8-12 weeks of age. All the assays were conducted between 10 am and 3 pm during the light phase. Independent cohorts of mice were tested in the three-chamber social interaction test, the open field test, and the buried food pellet test.

Three-chamber social interaction test: The three-chamber social interaction test was conducted as previously described (*32, 33*). All mice were tested in a nonautomated three-chambered box. Dividing walls had retractable doorways allowing access into each chamber. Mice were acclimated to the three-chambered box for 4 days before the test (10 min/day). On the test day, mice were transported to the testing room and habituated for at least 1 h before the experiment. A white noise generator was used to mitigate any unforeseen noises. The subject mouse was habituated in the chamber with two empty cylinders for 10 min. Then, the "toy" object was placed in one of the cylinders and mouse (stranger 1) was placed in another cylinder for the "sociability" trial. Mice were allowed to explore the chambers for 10 min. In the next "social novelty preference" trial, stranger 1 was kept in the cylinder as the familiar mouse and the toy object was replaced with a novel mouse (stranger 2). The subject mouse was again allowed to explore the chambers. During these two trials, mouse activities were recorded on video and the time spent sniffing each cylinder was manually measured. Preference index was calculated as follows. For sociability test: (sniffing time to mouse) x 100 / (sniffing time to mouse + sniffing time to object) - 50. For social novelty preference test: (sniffing time to novel mouse) x 100 / (sniffing time to novel mouse + sniffing time to familiar mouse) - 50.

Buried food pellet test: The buried food pellet test was performed as previously described (*34*). Mice were food-deprived for 24 h with free access to water. At the test, single mouse was placed in the test cage and allowed to freely explore the food pellets buried ~0.5 cm below the surface of a 3 cm-deep layer of beddings. Latency to find the hidden food pellet was measured. (n=11-18 mice per group).

Open field test: Novelty-induced activity in the open field was assessed as described previously (*33, 35*). Locomotion, rearing, and center time were measured for 10 min using a Photobeam Activity System (PAS–Open Field, San Diego Instruments). The PAS system consisted of two vertically stacked frames, each containing infrared lasers arranged in a 16 x 16 grid, which detected mouse movement, including ambulation and rearing. The open field box and surrounding photobeam apparatus were housed in a ventilated cabinet. Single-beam breaks were automatically recorded as "counts" and the PAS system automatically started recording counts once the mouse started moving. The total counts were recorded and the percentages of center counts (defined as those in the central 27.5 x 27.5 cm area) to total counts were calculated.

Serum collection and EV preparation

Blood (600-700 µl) was collected from mice via cardiac puncture under a deep anesthesia at time of sacrifice and placed at room temperature for 30 min. Sera were then separated by centrifugation at 300 x *g* for 5 min and stored at -80ºC for biochemical/molecular experiments or freshly used for *in vivo* experiments. For EV preparation, the sera were further centrifuged with 2,000 x *g* 10 min to remove platelets. EVs were prepared primarily with differential ultracentrifugation except for Supplementary **Figs 3, 5 and 6** where precipitation and size exclusion chromatography were also used as indicated. For EV enrichment with differential ultracentrifugation, the sera were centrifuged at 10,000 x *g* for 30 min at 4ºC to remove large vesicles. Then, the sera were diluted with PBS at 1:4 ratio and ultracentrifuged at 100,000 x *g* for 30 min at 4ºC using Optima MAX-XP ultracentrifuge with a TLA 120.2 rotor (k factor = 11) (Beckman Coulter) (*36*). The pellet was resuspended with 1 ml of PBS and ultracentrifuged at 100,000 x *g* for 30 min at 4ºC to wash, and then resuspended with 10 µL of PBS. For EV precipitation, the sera were processed with Total Exosome Isolation kit (Thermo Fisher Scientific) following the manufacturer's protocol and the EV-containing fraction was resuspended in 50 µL PBS. For EV enrichment with size exclusion chromatography, each serum

sample was applied to a 70 nm qEVsingle size exclusion column (Izon) and eluted with DPBS. Fractions were collected using an Izon automated fraction collector: following elution of a 1-ml void fraction, 0.5-ml fractions were collected, of which fractions 6 to 8 were enriched in EVs. These fractions were pooled, concentrated using Amicon 15 Ultra RC 100 kD filters, and aliquoted and stored in LoBind tubes (Eppendorf) at -80°C.

Transmission Electron Microscopy

Freshly prepared EV samples were adsorbed onto carbon-coated/palladium grids for 1 min and negatively stained with 2% (w/v) uranyl acetate for 1 min. EVs were visualized under a FEI Tecnai Spirit T12 transmission electron microscope (Thermo Fisher Scientific / FEI).

Nano particle tracking analysis (NTA)

Concentration and size distribution of particles in EV samples were analyzed with NanoSight NS300 (Malvern Panalytical) or ZetaView (Particle Metrix) following standard protocols (*37, 38*).

Adoptive cell transfer, serum injection, and EV injection,

For adoptive cell transfer, splenocytes and T cells were collected from spleen. T cells were isolated using the Pan T cell isolation kit II, mouse (#130-095-130, Miltenyi Biotech). T cells were >99%-positive for CD3ε expression by flow cytometry. Splenocytes (1 x 10^8 cells 100 µL per mouse) and T cells (1 x 10^7 cells 100 µL per mouse) were transferred intravenously into *Rag1*$^{-/-}$ mice via retro-orbital injection following a standard protocol (*39*). Sera (150 µL per mouse) and EVs (2 x 10^9 particle in 100 µL per mouse unless stated otherwise) were also transferred intravenously into WT and *Rag1*$^{-/-}$ mice via retro-orbital injection. In our method, the number of EVs recovered from 500 µL total venous blood was about 4 x 10^9 particles. Considering that the total blood volume of an adult mouse is 2 ml, our injection corresponds to about 12.5% volume of the total circulating EVs in the blood.

Western blot

EV and brain lysates were prepared with RIPA buffer, separated on NuPAGE Bis-Tris Mini Gel (Thermo Fisher Scientific / Life Technologies) with equal amounts of total proteins loaded into

each lane, and transferred to PVDF membrane (Millipore). After blocking in 5% skim milk/PBS-0.1% Tween® 20 (PBS-T) for 1 h, the membrane was incubated with the primary antibody overnight at 4°C and then incubated with the HRP or fluorescent secondary antibodies for 1 h at room temperature. Chemiluminescence and fluorescence gel images were captured by Image Quant LAS 4000 and LAS 500 imagers (GE Healthcare/Cytiva) and analyzed with ImageJ/Fiji software[4]. The following primary antibodies were used: rabbit anti-Alix (1:1,000, #ab186429, Abcam, RRID:_2754981), rabbit anti-Calnexin (1:1,000, #ADI-SPA-860-D, Enzo Life Science, RRID:_1061834), mouse anti-CD81 (1:1,000, #sc-166029, Santa Cruz Biotechnology, RRID: AB_2275892), armenian hamster anti-mouse CD81(1:1,000, #sc-18877, Santa Cruz Biotechnology, RRID: AB_627194), anti-Rag1 (1:1,000, #sc-5599, Santa Cruz Biotechnology, RRID: AB_2300670), goat anti-Rag2 (1:1,000, #sc-7623, Santa Cruz Biotechnology, RRID: AB_2175836), and mouse anti-β-actin (1:5,000, #sc-47778, Santa Cruz Biotechnology, RRID: AB_626632). Horse anti-mouse IgG HRP (1:10,000, #7076, Cell Signaling), goat anti-rabbit IgG HRP (1:10,000, #7074P2, Cell Signaling), and donkey anti-goat IgG HRP (1:10,000, #sc-2020, Santa Cruz Biotechnology, RRID: AB_631728) were used as secondary antibodies.

Flow cytometry

Flow cytometry of splenocytes was performed using a standard protocol (*39*). Single cell suspensions were obtained from spleens collected after PBS perfusion. After lysis of red blood cell with 1x RBC Lysis Buffer (Thermo Fisher Scientific/eBioscience), cells were washed with FACS buffer and Fc-blocked with anti-CD16/CD32 (#14-0161-82, Thermo Fisher Scientific/eBioscience, RRID: AB_467133). Then, cells were stained with the following antibodies: rat anti-CD3 APC (1:100, #100235 BioLegend, RRID: AB_2561455), rat anti-mouse CD19 PE (1:100, #115508, BioLegend, RRID: AB_313643), rat anti- B220 Alexa Fluor 488 (1:100, #103228, BioLegend, RRID: AB_492974). Flow cytometry was conducted using FACS Calibur, LSRII, or Accuri C6 cytometer (all from BD Biosciences) and analyzed with FlowJo software (FlowJo LLC).

DREADD experiments

Mice were stereotactically injected with 400 nl of pAAV-CamKIIa-hM4D(Gi)-mCherry ($4.4x10^{12}$ genomic copies/mL, #50477, Addgene) at the rate of 100 to 200 nl/min into the mPFC

bilaterally using a NanoFil syringe with a 35G blunt needle (WPI). The following stereotactic coordinate was used for injection; anteroposterior (AP): +1.8mm; mediolateral (ML): ± 0.3mm; and dorsoventral (DV): -2.1 mm from the bregma. Three to four weeks later, behavioral assays were conducted. CNO (10 mg/kg in 0.5% DMSO/PBS, #BML-NS105-0025, Enzo Life Sciences) was intraperitoneally injected 45 min prior to the three-chamber social interaction test. For the three-chamber social interaction test, mice were intraperitoneally injected with PBS during acclimation for 4 consecutive days and then injected with CNO or vehicle (0.5% DMSO/PBS) on the test day as previously described(*40*).

Brain collection

Mice were anesthetized and transcardially perfused with ice-cold PBS. For RNA-seq experiments, brains were dissected and stored at -80 ºC until use. For immunohistochemistry, mice were further perfused by 4% paraformaldehyde (PFA) and the dissected brains were fixed in ice-cold 4% PFA/PBS for 24 h.

Immunohistochemistry

Immunohistochemistry experiments were conducted as previously described (*33, 41*). Free floating coronal sections (40 μm in thickness) were prepared with a Leica cryostat and, if necessary, antigen retrieval was performed with 10 mM sodium citrate buffer (pH8.5). The sections were then placed in blocking solution (PBS supplemented with 2% Normal Goat Serum, 1% BSA, 0.1% TritonX, 0.05% Tween-20, and 0.05% sodium azide) for 1 h at room temperature and then incubated at 4°C overnight with the following primary antibodies: mouse anti-NeuN (1:500, #MAB377, Merck-Millipore, RRID: AB_2298772), rabbit anti-Iba1 (1:400, #019-19741, Wako Chemicals, RRID: AB_839504), goat anti-c-Fos (1:500, #sc-52, Santa Cruz Biotechnology, RRID: AB_2106783), rabbit anti-c-Fos (1:200, #9F6, Cell Signaling, RRID: AB_22472111), mouse anti-CaMKIIα (1:200, #688602, Clone 6G9, BioLegend, RRID: AB_2617027), rabbit anti-CaMKIIα (1:100, #20666, Proteintech, RRID:AB_2878722), rabbit anti-RFP (1:1,000, #600-401-379, Rockland, RRID: AB_2209751), rabbit anti-PKCε (1:100, #20877-1-AP, Proteintech, RRID:AB_10697812), mouse anti-CC1 (1:100, #OP80, Calbiochem, RRID:AB_2057371), rabbit anti-S100β (1:200, #ab868, Abcam, RRID:AB_306716), mouse anti-NSE (1:500, #66150, Proteintech, RRID:AB_2881546), mouse anti-Gephyrin (1:100,

#147021, Synaptic Systems, RRID:AB_2232546), and rabbit anti-$GABA_A R\gamma 2$ (1:100, #AGA-005, Alomone Labs). After washing with PBS, the sections were further incubated with fluorophore-conjugated secondary antibodies at 1:400 dilution for 2 h at room temperature, followed by DAPI staining (1:50,000, #10236276001, Roche) for 10 min at room temperature. were used for signal detection. The sections were mounted on glass slides with Permafluor™ mounting medium or ProLong Diamond antifade mounting medium (Thermo Fisher Scientific). Images were acquired using Zeiss LSM510, 700 and 800 confocal microscopes with Zen software (Carl Zeiss) or an Olympus BX61 epifluorescence microscope (Olympus).

EV labeling and brain distribution analysis

For chemical dye labeling of EVs, WT bEVs were stained with PKH26 lipophilic dye (Sigma-Aldrich). Briefly, EVs were suspended with 194 µl of Diluent C, mixed with 6 µl of PKH26 dye, and incubated for 5 min at room temperature. The reaction was stopped by adding 100 µl of 20% BSA. Then, the EV suspensions were applied to the Exosome Spin Column (Thermo Fisher Scientific) and spun down to remove excess amount of the dye. Next, stained EVs were diluted to 2×10^{10}/mL with DMEM medium (Thermo Fisher Scientific). For genetically labeling of EVs, EVs were collected from the sera of mTmG mice, in which cellular membranes and thus cell-derived EVs are labeled with membrane-anchored TdTomato. EVs (2×10^9 particles /mouse) were intravenously injected into recipient mice. Brains were collected 1 h later and PKH26 and TdTomato puncta were analyzed by immunohistochemistry.

Image analysis

Image analysis was performed as previously described (*33*). c-Fos quantification was conducted using Image J/Fiji software(*42*) and the percentages of c-Fos-expressing cells among NeuN neurons were calculated. Images were taken at 20x and 40x magnification. The maximal projection images of z-stacked images (14 sections at 0.75 µm) were used for quantification with confocal. Three to five brain sections from each animal were chosen based on anatomic landmarks to ensure that equivalent regions were analyzed. EV co-localization images with each cell type marker (NSE^+, $Iba1^+$, $S100\beta^+$, and $CC1^+$ cells) were taken with 63x magnification. The maximal projection images of z-stacked images (14 sections at 0.34 µm) were used for quantification. The co-localization was defined when at least one EV puncta were overlapped

with the cell marker staining. The percentages of EV-positive cells among all the cells for each cell type was quantified per visual field and averaged across 4-5 independent fields to calculate %EV-positive cells/total cells. For synaptic GABA receptor quantification, images were taken using a 63x magnification objective with 2x optical zoom. The maximal projection images of z-stacked images (14 sections at 0.34 μm) were used for quantification. Postsynaptic $GABA_AR\gamma2$ was determined by the co-localized puncta of $GABA_AR\gamma2$ and gephyrin on the soma of $CaMKII\alpha^+$ neurons. The number of $GABA_AR\gamma2^+$ $gephyrin^+$ puncta per $CaMKII\alpha^+$ neurons was counted and averaged across 5-6 $CaMKII\alpha^+$ neurons per mouse.

RNA-seq

Total RNAs were extracted from frontal cortices of mice transcardially perfused with ice-cold PBS using RNeasy micro kit (Qiagen). Libraries were prepared with NEB Next Ultra II Directional RNA Library Prep kit (New England BioLabs) and a 75-bp paired-end sequencing was performed on a NextSeq500 (Illumina) at the UAB Genomics Core. Raw RNA sequencing reads were aligned to the mouse reference genome (GRCm38 p6, Release M24) from Gencode with STAR (version 2.7.5c) (using parameters --outReadsUnmapped Fastx --outSAMtype BAM SortedByCoordinate --outSAMattributes All)(*43*). Following alignment, HTSeq-count (version 0.12.3) was used to count the number of reads mapping to each gene (using parameters -r pos -t exon -i gene_id -a 10 -s no -f bam)(*44*). Normalization and differential expression were then applied to the count files using DESeq2 (version 1.28.1) following their vignette(*45*). Lists were compiled of genes whose expression was significantly altered between *Rag1*$^{-/-}$ mice and WT mice, and between *Rag1*$^{-/-}$ mice with and without WT EVs. P values were adjusted using the Benjamini-Hochberg false discovery rate (FDR) and adjusted $p < 0.05$ was considered statistically significant. Then, genes whose expression changes were overlapped were extracted for the downstream analysis. Gene ontology (GO) enrichment analysis was performed using Metascape(*46*), including biological process (BP), molecular function (MF) and cellular component (CC).

miRNA-seq

Total RNAs containing small RNA fractions were extracted from EVs enriched with differential ultracentrifugation using miRNeasy mini kit (Qiagen). Libraries were prepared with Qiagen

miRNA library prep kit (Qiagen) and a 75-bp single-end sequencing was performed on a NextSeq500 (Illumina) at the UAB Genomics Core. Raw miRNA-Seq FASTQ reads were uploaded to Qiagen's GeneGlobe Data Analysis Center (https://geneglobe.qiagen.com/us/analyze/) for analysis. Briefly, the reads were trimmed, unique molecular identifier (UMI) sequences identified, and then aligned to miRbase (ver21)(*47*) and the mouse mm10 genome. This created a tab-delimited file containing the count reads and UMIs assigned to each miRNA. The UMIs were then normalized, and differential expression was calculated using DESeq2. For miRNA over-representation analysis, we curated the previous publications (at least 2 publications for one mouse model) and established the altered miRNA lists from several mouse models with sociability impairment(*48-72*). The lists of miRNAs were converted to ver21 with miRBaseConverter(*73*). Enrichment of altered miRNAs was analyzed with Fisher's exact test. P values from multiple testing were adjusted (q-value) using the Benjamini-Hochberg false discovery rate (FDR) with a significant level of 0.05. For pathway analysis of potential target genes of miRNAs, target genes of miRNAs were obtained with miRTarBase and TargetScan 8.0 (*74, 75*). GO enrichment analysis of miRNA target genes was performed using Metascape as described above.

Brain slice electrophysiology

Adult mice were anesthetized through isoflurane inhalation and then decapitated. The brain was quickly removed and coronal mPFC slices of 300 μm were obtained using a Leica VT1200S vibratome. The dissection buffer used for the slicing was at pH 7.3 and 305 mOsm, containing the following (in mM): 206 sucrose, 25 $NaHCO_3$, 2.5 KCl, 10 $MgSO_4$, 1.45 NaH_2PO_4, 0.5 $CaCl_2$, and 11 d-glucose). This buffer was kept oxygenated (5% CO_2–95% O_2) during the whole dissection. Slices were then transferred to a holding chamber containing artificial cerebrospinal fluid solution (aCSF), composed of the following (in mM): 126 NaCl, 26 $NaHCO_3$, 2.5 KCl, 1.45 NaH_2PO_4, 1 $MgCl_2$, 2 $CaCl_2$, and 9 d-glucose. Slices were kept oxygenated at room temperature (22–25 °C) for at least 1 h. After this resting period, they were transferred to a submersion-type recording chamber upon a modified microscope stage, and kept constantly perfused with oxygenated aCSF throughout the experiments. The temperature in the recording chamber was kept at 30 ± 1.5 ºC using an inline heater (Warner Instruments). Recording electrodes pipettes were fabricated from borosilicate glass with input resistances of ~4–7 MΩ.

We used a visualized slice setup under a differential interference contrast-equipped microscope to perform our electrophysiology experiments. Whole-cell patch-clamp recordings were made in neurons visually located in layer 5 of the prelimbic region of the mPFC. Spontaneous postsynaptic currents were recorded in voltage-clamp mode by using the SutterPatch double IPA system and SutterPatch software. We applied holding at -70 mV, and compensated the electrode and cell capacitance. For all experiments, recordings were taken only 5 minutes after the whole-cell configuration was achieved, to allow cell adaptation. Currents were recorded for 5 minutes for all experiments. We included in our data only recordings from cells in which the access resistance did not change more than 20% during the recording and that displayed relatively stable baselines. Synaptic currents were detected and measured using SutterPatch software in-built system for analysis, and average amplitude e frequency of events for each cell was taken for statistical analysis. For sEPSC experiments, the $GABA_A$ antagonist bicuculline at 20 µM plus the NMDA antagonist D-APV at 50 µM were added to the bath, to isolate AMPA currents. The intracellular solution used was K^+ based and contained the following (in mM): 117 K-gluconate, 10 HEPES, 2 Na_2ATP, 0.4 Na_2GTP, 1 $MgCl_2$, 0.1 EGTA, 13 KCl, 0.07 $CaCl_2$, at pH 7.3, and 290 mOsm. For sIPSC experiments, the AMPA antagonist DNQX at 20 µM plus the NMDA antagonist D-APV at 50 µM were added to the bath, to isolate GABAergic currents. The intracellular solution used was Cs based and contained the following (in mM): 140 CsCl, 10 HEPES, 2 Na_2ATP, 0.4 Na_2GTP, 1 $MgCl_2$, 0.05 EGTA, 3.6 NaCl, at pH 7.3, and 290 mOsm. For the experiments where EVs were used, we added the EVs directly to the bath at a concentration of 2 $x10^7$ particles/ml (2 x 10^9 particles per slice), and slices were incubated with EVs for at least one hour before starting the experiments. Recordings were taken while constantly perfused by this aCSF with the EVs added.

RNase and detergent treatment of EVs

EVs were mixed with or without 1 µl RNaseA (ThermoFisfer, EN0531) and 10 µl Triton X-100 (Sigma, T2199) and adjusted up to 200 µl by PBS. All samples were then incubated at 37 °C for 30 min, followed by heat inactivation of RNase at 95 °C for 10 min. After samples had cooled, RNA was extracted using miRNEasy mini kit (Qiagen) according to the manufacturer's protocol.

Quantitative reverse-transcription PCR (qRT-PCR) of miRNAs

EV-derived RNA (30 ng) was used to synthesize cDNA using miRCURY LNA RT kit (Qiagen). The cDNAs were then diluted at 1:30 and qPCR was performed using 2x miRCURY SYBR Green master mix (Qiagen) and miRCURY LNA miRNA PCR Assays (#339306, YP00204772 for miR-23a-3p and #339306, YP00204063 for miR-103-3p, Qiagen) with 95 °C for 2 min, 50 cycles of 95 °C for 10 s, and 56 °C for 60 s, on a C1000 Touch Thermal Cycler with CFX96 Real Time PCR Detection System (Bio-Rad). Cycle threshold (Ct) values were averaged across triplicates per experiment and per target. ΔCt was calculated to compare the data between groups.

EV small RNA extraction and supplementation to other EVs

Small RNAs were extracted from EVs using miRNEasy mini kit (#217004, Qiagen). The extracted RNAs (25 ng) were mixed with 2 x 10^9 EV particles using Exo-Fect Exosome transfection kit. EVs loaded with small RNAs were then reconstituted with 100 µl of DMEM media and transferred intravenously into recipient mice via retro-orbital injection.

EV loading with miR-23a-3p and miR-103a-3p mimics

miRNA mimic of 23a-3p (250 pmol, #339173 YM00470983-ADA, Qiagen) and 103a-3p (250 pmol, ##339173 YM 00470828-ADA, Qiagen) or negative control (500 pmol, #339173 YM00479902-ADA, Qiagen) were mixed with 2 x 10^9 EV particles using Exo-Fect Exosome transfection kit (#EXFT20A-1, System Biosciences) according to the manufacturer's instruction. EVs containing miRNAs or negative controls were re-constituted with 100 µl of Dulbecco's Modified Eagle Medium (#11965-092, Gibco) and then injected intravenously into recipient mice.

Statistical analysis

Data were analyzed with Student's *t* test, and one-way ANOVA using GraphPad Prism 7 (GraphPad Software) and R. *Post hoc* analyses for one-way ANOVA were per- formed using Sidak's method, respectively. For pairwise tests, $p < 0.05$ was considered statistically significant. For tests with multiple comparisons, adjusted $p < 0.05$ was considered statistically significant.

Figure S1

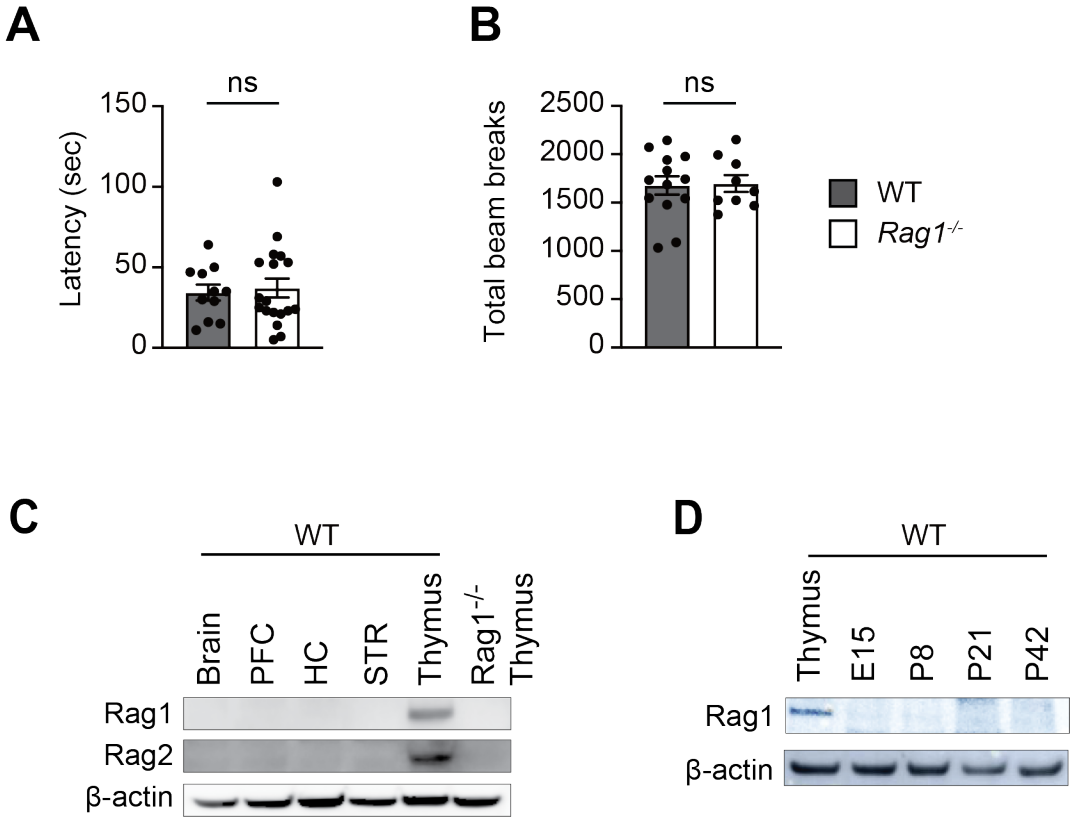

Figure S1: Additional behavioral data of *Rag1*$^{-/-}$ mice and Rag protein expression in the brain.

A, No difference in latency to find a buried food pellet in the buried food pellet test between WT and *Rag1*$^{-/-}$ mice. WT mice, n = 11 *Rag1*$^{-/-}$ mice, n = 18. **B**, No difference in total activities analyzed with the open field test between WT and *Rag1*$^{-/-}$ mice. WT mice, n = 13 *Rag1*$^{-/-}$ mice, n = 9. **C**, Western blot images showing no detectable Rag1 and Rag 2 proteins in the brains of WT mice. PFC, prefrontal cortex; HC, hippocampus; STR, striatum. **D**, Western blot images showing Rag1 and β-actin proteins in the thymus and brains of WT mice (embryonic day 15 (E15), postnatal day 8 (P8), P21, and P42. Each bar in the graphs represents mean ± SE. ns, not significant. Significance was determined by Student's *t*-test. See Supplementary Table 12 for the detail of statistical analysis.

Figure S2

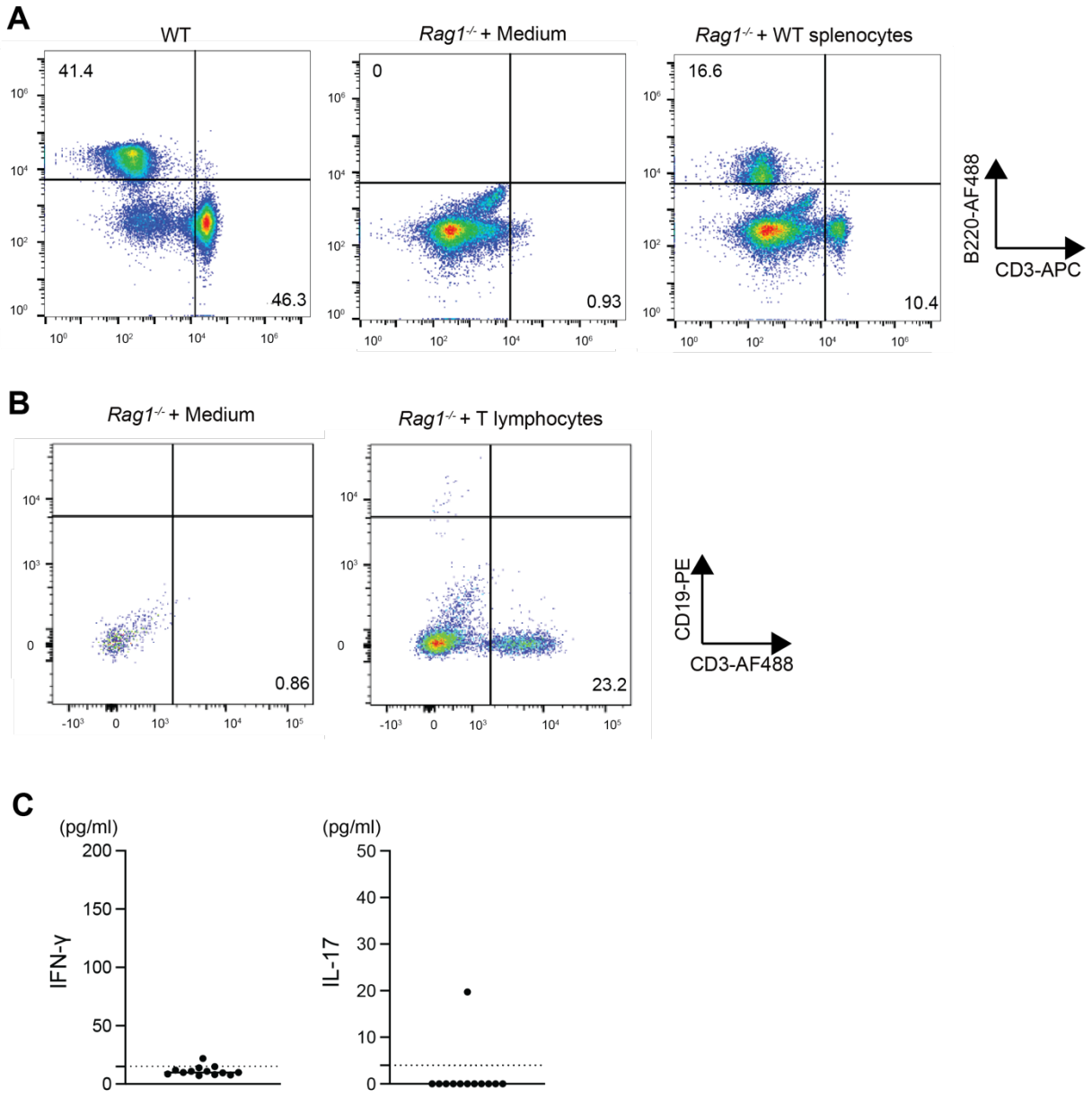

Figure S2: Lymphocyte reconstitution after adoptive cell transfer

A, Flow cytometry data showing the recovery of $CD3^+$ T cells and $B220^+$ B cells in *Rag1*$^{-/-}$ mice adoptively transferred with WT splenocytes. **B**, Flow cytometry data showing the recovery of $CD3^+$ T cells in *Rag1*$^{-/-}$ mice adoptively transferred with WT T cells. **C**, ELISA data showing the levels of IFN-γ and IL-17 in WT mouse sera.

Figure S3

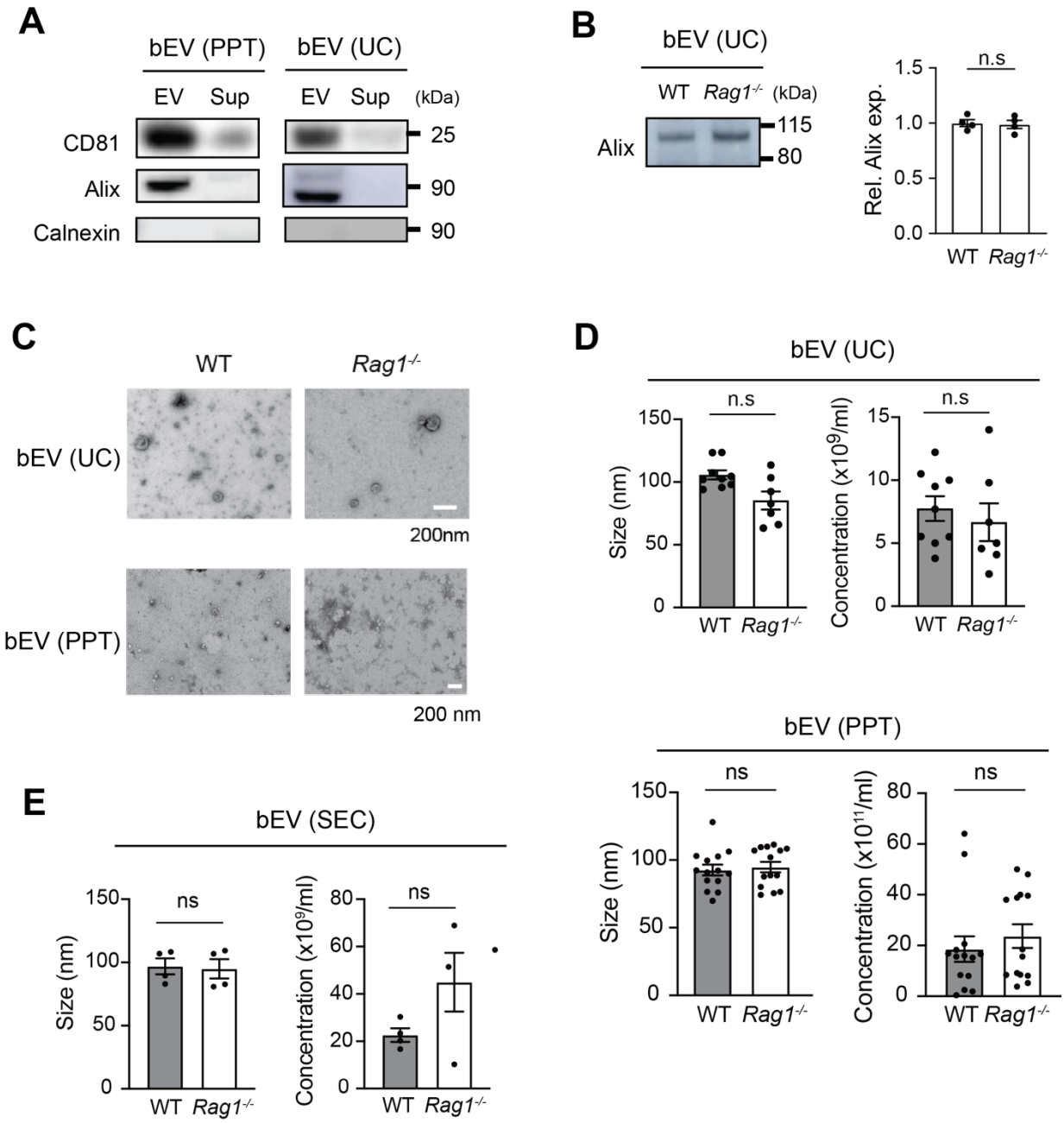
A
bEV (PPT)
bEV (UC)
EV
Sup
EV
Sup
(kDa)
CD81
Alix
Calnexin
25
90
90
B
bEV (UC)
WT
Rag1-/-
(kDa)
Alix
115
80
n.s
Rel. Alix exp.
1.5
1.0
0.5
0.0
WT
Rag1-/-
C
WT
Rag1-/-
bEV (UC)
200nm
bEV (PPT)
200 nm
D
bEV (UC)
n.s
n.s
Size (nm)
150
100
50
0
Concentration (x10^9/ml)
15
10
5
0
WT
Rag1-/-
WT
Rag1-/-
bEV (PPT)
ns
ns
Size (nm)
150
100
50
0
Concentration (x10^11/ml)
80
60
40
20
0
WT
Rag1-/-
WT
Rag1-/-
E
bEV (SEC)
ns
ns
Size (nm)
150
100
50
0
Concentration (x10^9/ml)
80
60
40
20
0
WT
Rag1-/-
WT
Rag1-/-

Figure S3: Characterization of bEVs prepared with several methods.

A, Western blot images of EV marker proteins, CD81 and Alix, in bEVs prepared with precipitation (PPT) and differential ultracentrifugation (UC). Calnexin, a cytoplasmic protein marker. Sup, supernatants after EV precipitations. **B**, Equal levels of expression for EV marker protein, Alix, in WT and *Rag1*$^{-/-}$ samples (n=3 per group). Left, representative Western blot images. Right, quantification graphs showing no difference in expression levels between WT and *Rag1*$^{-/-}$ samples. Equal amounts of proteins were loaded into each lane. **C**, Representative TEM images of bEVs prepared with UC and PPT. Scale bar = 200 nm. **D**, NanoSight® analysis of bEVs prepared with UC and PPT from WT and *Rag1*$^{-/-}$ mouse sera. WT, n = 13; *Rag1*$^{-/-}$, n = 11. **E**, ZetaView® analysis of bEVs prepared with size exclusion chromatography (SEC) from WT and *Rag1*$^{-/-}$ mouse sera. WT, n = 4; *Rag1*$^{-/-}$, n = 4. Each bar in the graphs represents mean ± SE. ns, not significant. Significance was determined by Student's *t*-test. See Supplementary Table 12 for the detail of statistical analysis.

Figure S4

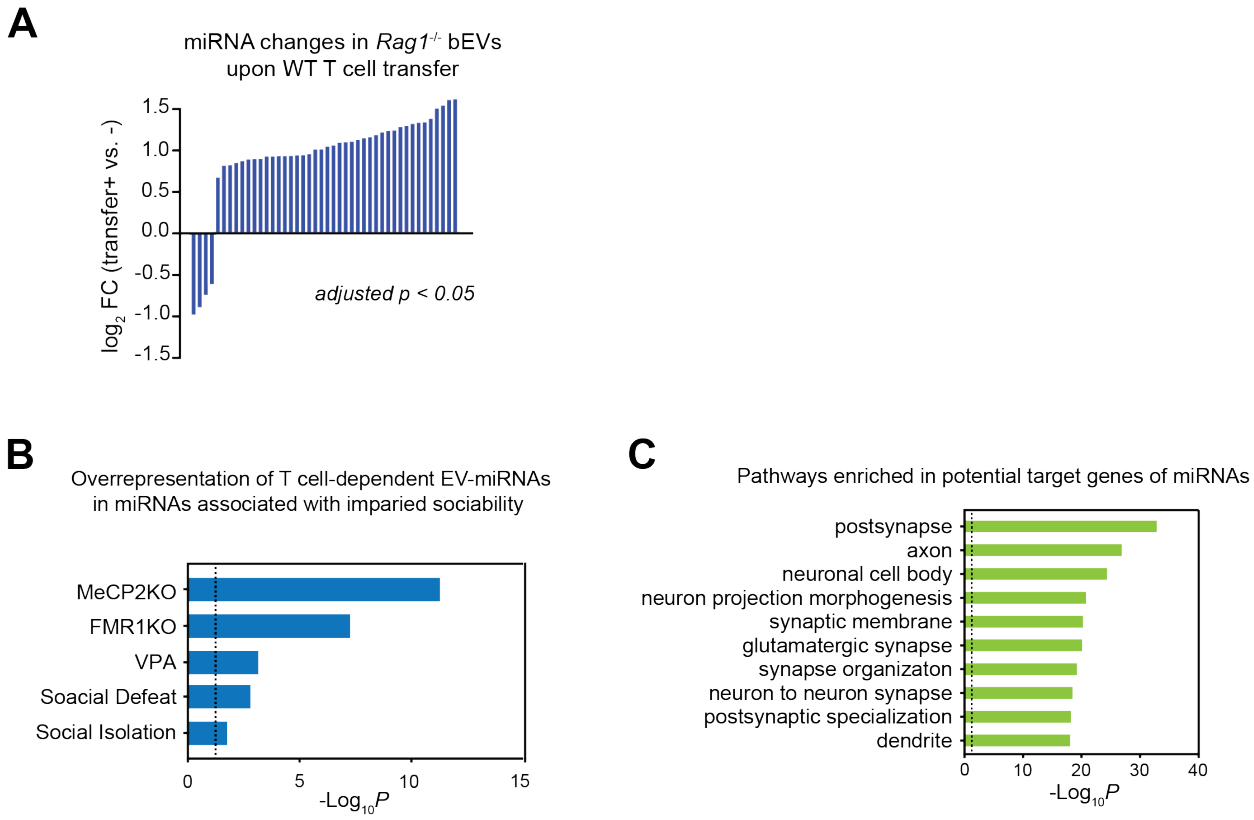

Figure S4: miRNA expression changes in *Rag1*$^{-/-}$ bEVs upon WT T cell transfer

A, Waterfall plot representing the bEV miRNAs whose expression significantly changed (adjusted $p < 0.05$) by the adoptive transfer of WT T cells into *Rag1*$^{-/-}$ mice. These miRNAs are regarded as T cell-dependent EV-miRNAs. *Rag1*$^{-/-}$ mice, n = 6; *Rag1*$^{-/-}$ mice + WT T cells, n = 6**.** **B,** T cell-dependent EV miRNAs were over-represented by the miRNAs whose expression changes were previously observed in the mice with sociability deficits. The list of miRNAs were curated from the previous publications (at least 2 publications for each mouse model) on several mouse models with sociability impairment (*48-72*). Enrichment was calculated with Fisher's exact test. **C,** Potential target genes of T cell-dependent EV miRNAs were enriched in the regulation of synapses and neurons.

Figure S5

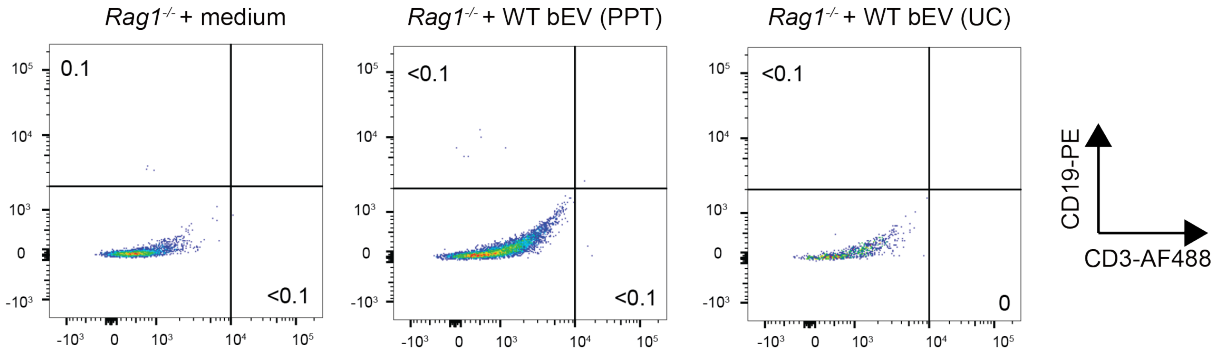

Figure S5: No recovery of T and B cells in *Rag1*$^{-/-}$ mice intravenously injected with bEVs from WT mice.

No changes in T or B cell populations were detected in the spleen from *Rag1*$^{-/-}$ mice after intravenous injection with bEVs from WT mice.

Figure S6

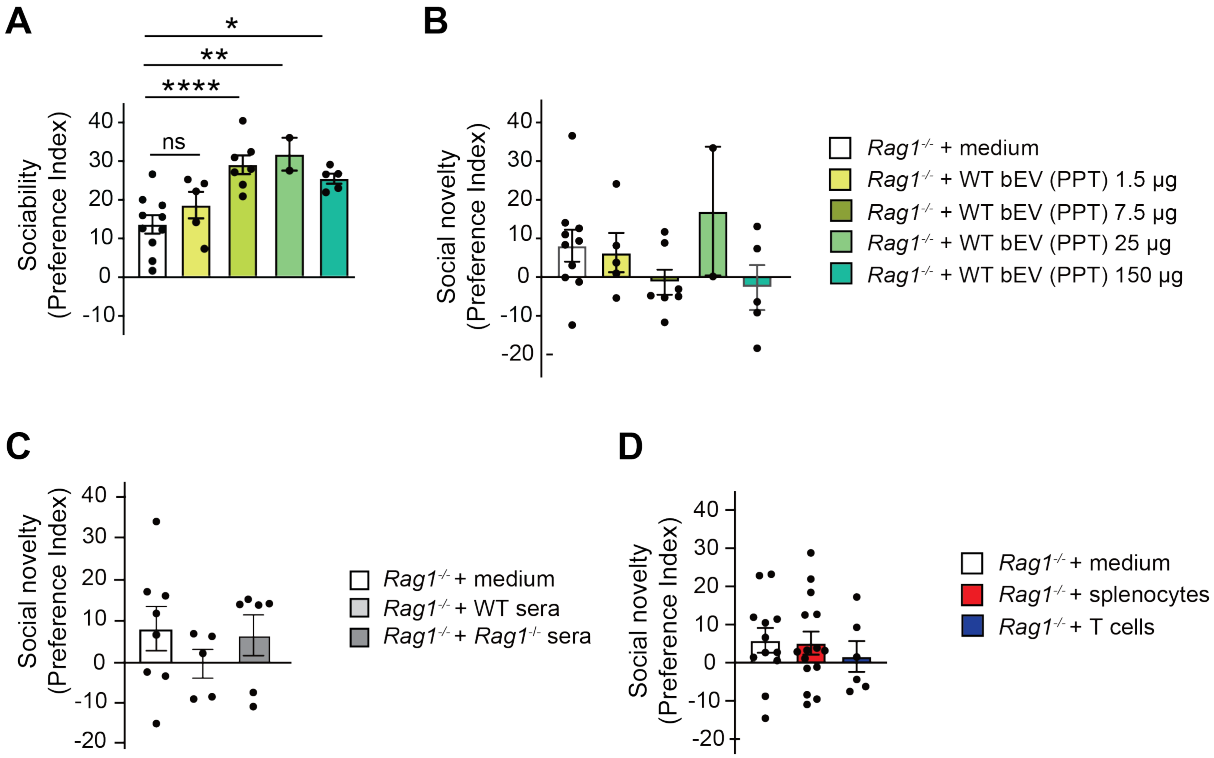

Figure S6: No recovery in social novelty preference by *Rag1*$^{-/-}$ mice after intravenous injection with WT bEVs or adoptive transfer of WT splenocytes or T cells.

A, B, Intravenous injection of WT bEVs (enriched by PPT) into *Rag1*$^{-/-}$ mice ameliorated their sociability deficits, but not social novelty preference deficits. *Rag1*$^{-/-}$ mice + medium, n = 10; *Rag1*$^{-/-}$ mice + WT bEVs 1.5 μg, n = 5; *Rag1*$^{-/-}$ mice + WT bEVs 7.5 μg, n = 7; *Rag1*$^{-/-}$ mice + WT bEVs 25 μg, n = 2; and *Rag1*$^{-/-}$ mice + WT bEVs 150 μg, n = 5. **C**, Intravenous injection of WT and *Rag1*$^{-/-}$ sera into *Rag1*$^{-/-}$ mice did not show any rescue effect on their social novelty preference deficits. *Rag1*$^{-/-}$ mice + medium, n = 8; *Rag1*$^{-/-}$ mice + WT sera, n = 5; *Rag1*$^{-/-}$ mice + *Rag1*$^{-/-}$ sera, n = 6. **D**, Adoptive transfer of neither splenocytes nor T cell reconstitution on *Rag1*$^{-/-}$ mice showed any rescued effect on their social novelty preference deficits. *Rag1*$^{-/-}$ mice + medium, n = 12; *Rag1*$^{-/-}$ mice + WT splenocytes, n = 15; *Rag1*$^{-/-}$ mice + WT T cells, n = 6. Each bar in the graphs represents mean ± SE. ns, not significant. *p<0.05, **p<0.01, ****p <0.001. Significance was determined by one-way ANOVA with *post hoc* Dunnett's test. See Supplementary Table 12 for the detail of statistical analysis.

Figure S7

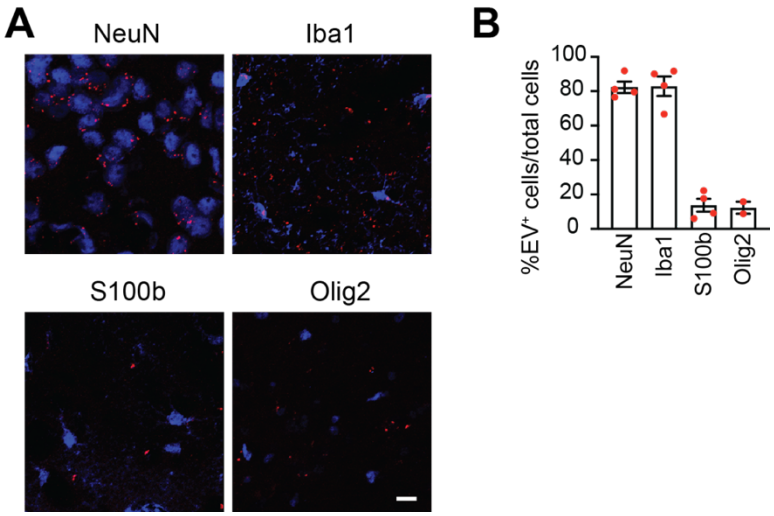

Figure S7: Co-localization of PKH26-labeled bEVs with neurons and microglia.

A, Representative confocal microscope images showing the localization of PKH26-labeled bEVs with NeuN^{+} neurons and Iba1^{+} microglia in the mPFC of *Rag1*$^{-/-}$ mice. **B,** Quantification of PKH26-labeled bEVs localized with NeuN^{+} neurons, Iba1^{+} microglia, S100b^{+} astrocytes, and Olig2^{+} oligodendrocyte-lineage cells in the mPFC of *Rag1*$^{-/-}$ mice, n = 3. Scale bar, 10 µm. Each bar in the graphs represents mean ± SE.

Figure S8

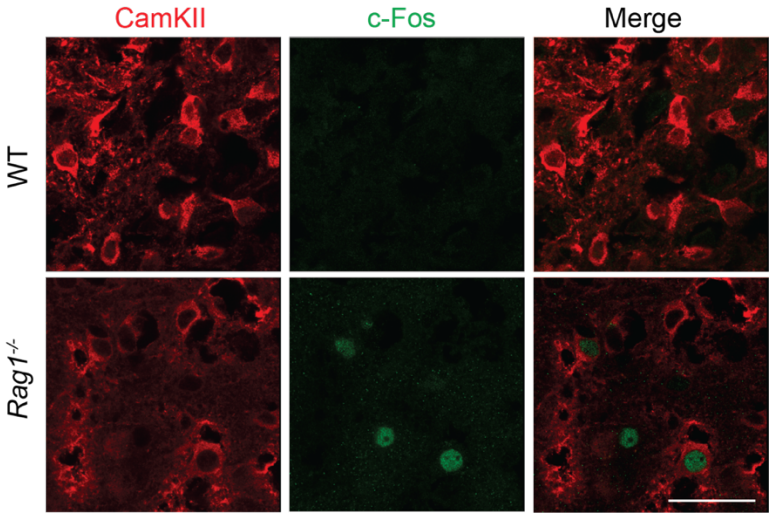

Figure S8: Increased cFos expression in CaMKIIα^{+} neurons in the mPFC of *Rag1*$^{-/-}$ mice. Representative images of c-Fos immunoreactivities in CaMKIIα^{+} neurons in the mPFC of *Rag1*$^{-/-}$ mice compared with WT mice. Scale bar, 50 μm.

Figure S9

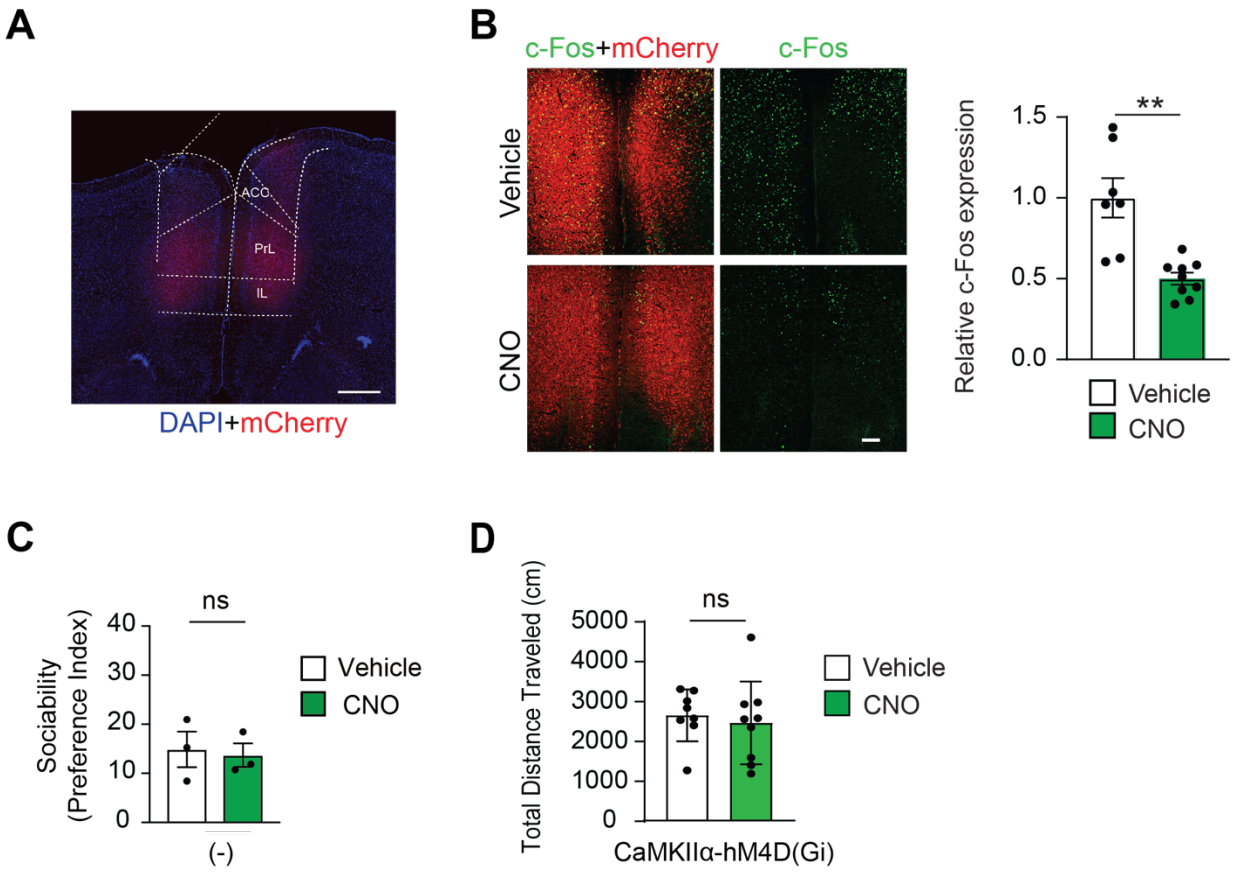

Figure S9: Validation of DREADD experiments for chemogenic inhibition of CaMKIIα^{+} neurons in the mPFC of *Rag1*$^{-/-}$ mice.

A, Representative image of AAV-CaMKIIα-hM4D(Gi)-mCherry expression in the mPFC of *Rag1*$^{-/-}$ mice. Scale bar, 500 µm. **B**, c-Fos immunoreactivities were suppressed in CNO injected group compared with Vehicle injected group. Vehicle n = 3; CNO n = 3. **C**, No impact of CNO injections on sociability behaviors in *Rag1*$^{-/-}$ mice lacking the expression of DREADD construct. **D**, No significant changes in total travel distance during sociability assays in *Rag1*$^{-/-}$ mice expressing DREADD construct upon CNO injections. Scale bar, 50 µm. Each bar in the graphs represents mean ± SE. $^{**}p<0.01$. Significance was determined by Student's *t*-test. See Supplementary Table 12 for the detail of statistical analysis.

Figure. S10

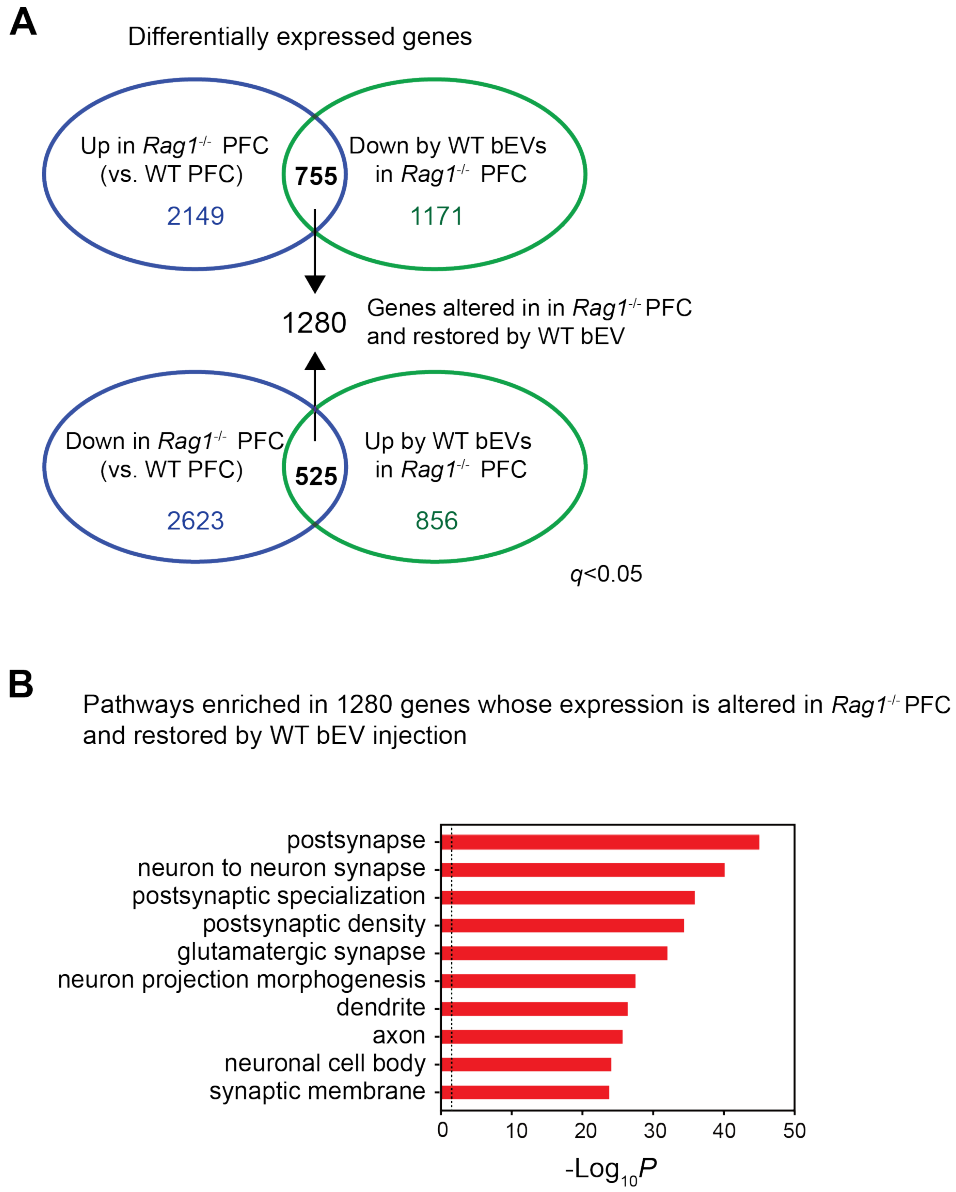

Figure S10: WT bEVs restore impaired synaptic gene expression in the mPFC of *Rag1*$^{-/-}$ mice.

A, Venn diagram showing the numbers of differentially expressed genes in the mPFC of *Rag1*$^{-/-}$ mice compared to WT mice and those in the mPFC of *Rag1*$^{-/-}$ mice with WT bEV injection compared to *Rag1*$^{-/-}$ mice with medium injection. WT mice, n = 3; *Rag1*$^{-/-}$ mice, n = 3; *Rag1*$^{-/-}$ mice + WT bEVs, n = 3. **B,** Pathway enrichment analysis of 1280 genes whose expression were altered in opposite directions between WT vs *Rag1*$^{-/-}$ and *Rag1*$^{-/-}$ vs *Rag1*$^{-/-}$ + WT bEV comparisons.

Figure S11

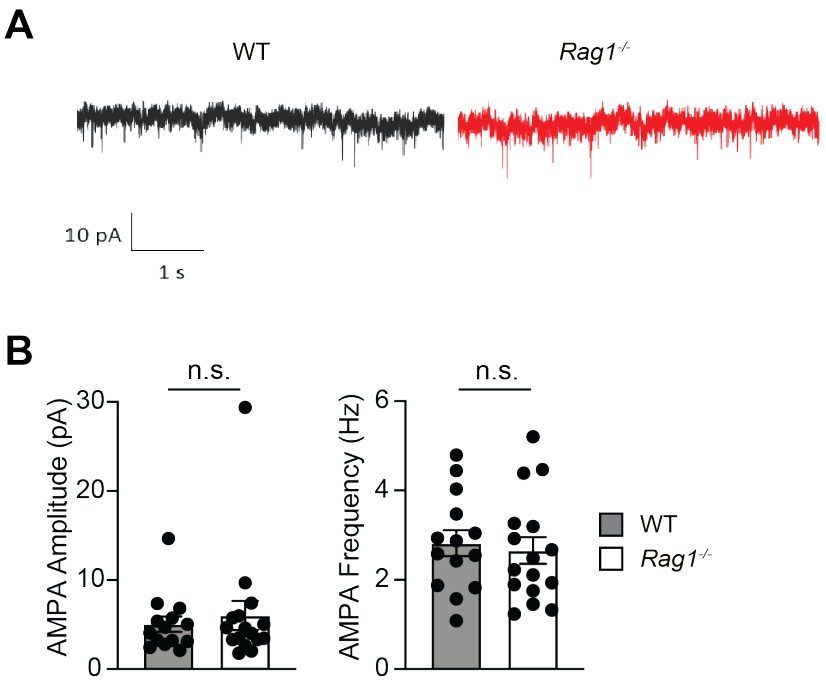

Figure S11: No changes in spontaneous excitatory AMPAR signaling in the mPFC layer V pyramidal neurons of *Rag1*$^{-/-}$ mice.

A, Representative traces of a gap free recording of layer V pyramidal neurons in the PrL. sEPSCs through AMPA receptors can be seen. Recordings were made in the presence of AP-V (50 µM). **B,** No significant difference in the amplitudes or the frequencies of AMPA currents between WT and *Rag1*$^{-/-}$ mice. Each bar in the graphs represents mean ± SE. Sample size was 3 adult male animals per group, with recorded cells used as the statistical unit for analysis. Significance was determined by Student's *t*-test. ns, not significant.

Figure S12

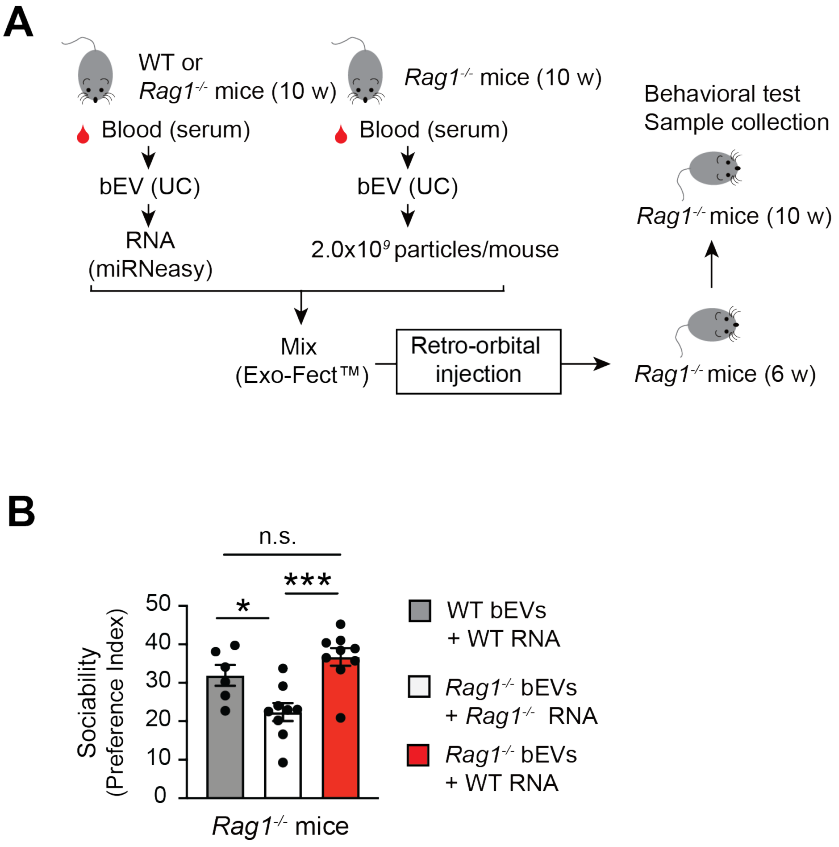

Figure S12: Differential effects of bEV-derived RNAs.

A, Experimental outline of bEV collection, intravenous injection, and subsequent behavioral assay. **B**, Sociability data of *Rag1*$^{-/-}$ mice administered with WT bEVs + WT RNA, *Rag1*$^{-/-}$ bEVs + *Rag1*$^{-/-}$ RNA, and *Rag1*$^{-/-}$ bEVs + WT RNA. WT bEVs + WT RNA, n = 6; *Rag1*$^{-/-}$ bEVs + *Rag1*$^{-/-}$ RNA, n = 9; *Rag1*$^{-/-}$ bEVs + WT RNA, n = 9. Each bar in the graphs represents mean ± SE. *p<0.05, ***p<0.001. ns, not significant. Significance was determined by Student's t-test. See Supplementary Table 12 for the detail of statistical analysis.

Figure S13

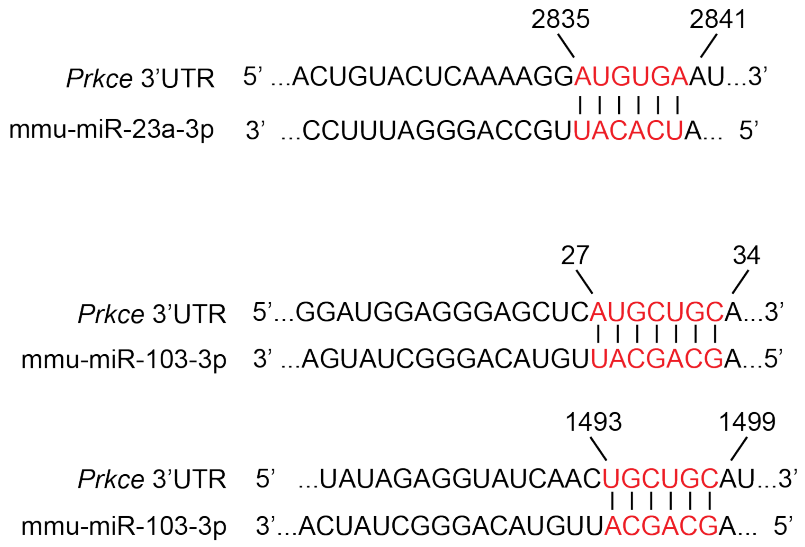

Figure S13: Predicted targeting sites for miR-23a-3p and miR-103-3p in the 3' UTR of *Prkce* gene. Predicted consequential pairings of target region (top) and miRNA (bottom) are shown for miR-23a-3p and miR-103-3p. The target regions are conserved between mouse and human. Prediction data were obtained using TargetScan (release 8.0: September 2021).

Figure S14

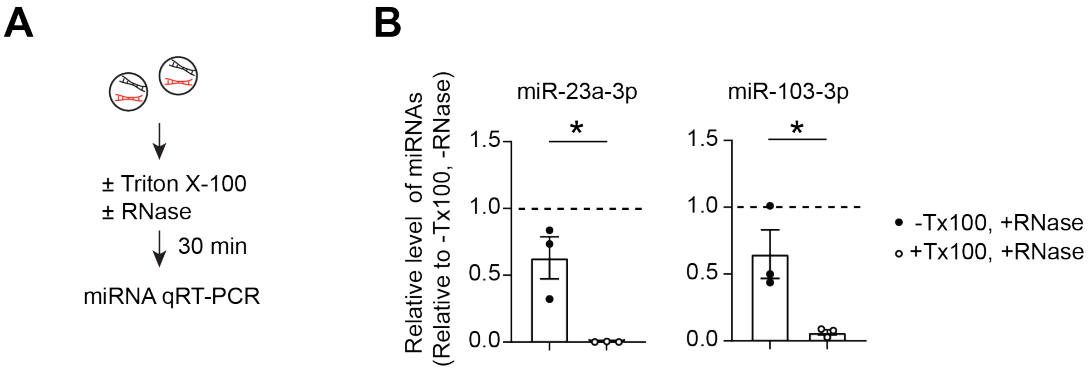

Figure S14: EV-associated miR-23a-3p and miR-103-3p are protected from RNase-dependent degradation.

A, Experimental procedures for Triton-X100 and RNase treatments of bEVs. **B**, Quantitative reverse-transcription PCR (qPCR) data of miR-23a-3p and miR-103-3p expression in WT bEV fractions treated as in **A.** Each bar in the graphs represents mean ± SE. *p<0.05. Significance was determined by Student's t-test. See Supplementary Table 12 for the detail of statistical analysis.

Figure S15

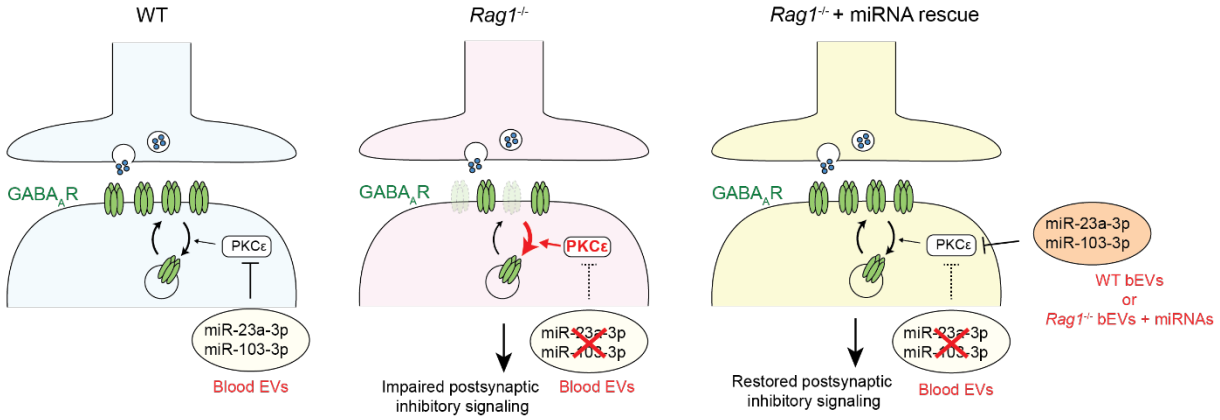

Figure S15: Schematic illustration of the mechanisms of how WT bEVs and miRNAs restore postsynaptic inhibitory signaling.

Rag1$^{-/-}$ mice lack miR-23a-3p and miR-103-3p supply from blood circulating EVs, resulting in enhanced expression of PKCε proteins, reduced synaptic expression of $GABA_A$ receptors, and impaired postsynaptic inhibitory signaling. WT bEVs or *Rag1*$^{-/-}$ bEVs supplemented with miR-23a-3p and miR-103-3p reverse this dysregulation.

References

1. S. A. Villeda *et al.*, Young blood reverses age-related impairments in cognitive function and synaptic plasticity in mice. *Nat Med* **20**, 659-663 (2014).
2. J. M. Castellano *et al.*, Human umbilical cord plasma proteins revitalize hippocampal function in aged mice. *Nature* **544**, 488-492 (2017).
3. A. J. Filiano *et al.*, Unexpected role of interferon-gamma in regulating neuronal connectivity and social behaviour. *Nature* **535**, 425-429 (2016).
4. S. M. Clark, C. N. Vaughn, J. A. Soroka, X. Li, L. H. Tonelli, Neonatal adoptive transfer of lymphocytes rescues social behaviour during adolescence in immune-deficient mice. *Eur J Neurosci* **47**, 968-978 (2018).
5. M. D. Reed *et al.*, IL-17a promotes sociability in mouse models of neurodevelopmental disorders. *Nature* **577**, 249-253 (2020).
6. M. Yanez-Mo *et al.*, Biological properties of extracellular vesicles and their physiological functions. *J Extracell Vesicles* **4**, 27066 (2015).
7. G. van Niel, G. D'Angelo, G. Raposo, Shedding light on the cell biology of extracellular vesicles. *Nat Rev Mol Cell Biol* **19**, 213-228 (2018).
8. H. Valadi *et al.*, Exosome-mediated transfer of mRNAs and microRNAs is a novel mechanism of genetic exchange between cells. *Nat Cell Biol* **9**, 654-659 (2007).
9. J. C. Gross, V. Chaudhary, K. Bartscherer, M. Boutros, Active Wnt proteins are secreted on exosomes. *Nat Cell Biol* **14**, 1036-1045 (2012).
10. K. O'Brien, K. Breyne, S. Ughetto, L. C. Laurent, X. O. Breakefield, RNA delivery by extracellular vesicles in mammalian cells and its applications. *Nat Rev Mol Cell Biol* **21**, 585-606 (2020).
11. F. J. Verweij *et al.*, The power of imaging to understand extracellular vesicle biology in vivo. *Nat Methods* **18**, 1013-1026 (2021).
12. K. Ridder *et al.*, Extracellular vesicle-mediated transfer of genetic information between the hematopoietic system and the brain in response to inflammation. *PLoS Biol* **12**, e1001874 (2014).
13. T. Thomou *et al.*, Adipose-derived circulating miRNAs regulate gene expression in other tissues. *Nature* **542**, 450-455 (2017).
14. A. M. Dickens *et al.*, Astrocyte-shed extracellular vesicles regulate the peripheral leukocyte response to inflammatory brain lesions. *Sci Signal* **10**, (2017).
15. M. D. Muzumdar, B. Tasic, K. Miyamichi, L. Li, L. Luo, A global double-fluorescent Cre reporter mouse. *Genesis* **45**, 593-605 (2007).
16. O. Yizhar *et al.*, Neocortical excitation/inhibition balance in information processing and social dysfunction. *Nature* **477**, 171-178 (2011).
17. L. K. Bicks, H. Koike, S. Akbarian, H. Morishita, Prefrontal Cortex and Social Cognition in Mouse and Man. *Front Psychol* **6**, 1805 (2015).
18. P. Chen, W. Hong, Neural Circuit Mechanisms of Social Behavior. *Neuron* **98**, 16-30 (2018).

19. O. Yizhar, D. R. Levy, The social dilemma: prefrontal control of mammalian sociability. *Curr Opin Neurobiol* **68**, 67-75 (2021).
20. B. L. Roth, DREADDs for Neuroscientists. *Neuron* **89**, 683-694 (2016).
21. C. Castano, M. Mirasierra, M. Vallejo, A. Novials, M. Parrizas, Delivery of muscle-derived exosomal miRNAs induced by HIIT improves insulin sensitivity through down-regulation of hepatic FoxO1 in mice. *Proceedings of the National Academy of Sciences of the United States of America* **117**, 30335-30343 (2020).
22. W. H. Chou *et al.*, GABAA receptor trafficking is regulated by protein kinase C(epsilon) and the N-ethylmaleimide-sensitive factor. *J Neurosci* **30**, 13955-13965 (2010).
23. M. J. Shurtleff, M. M. Temoche-Diaz, K. V. Karfilis, S. Ri, R. Schekman, Y-box protein 1 is required to sort microRNAs into exosomes in cells and in a cell-free reaction. *Elife* **5**, (2016).
24. B. Barman *et al.*, VAP-A and its binding partner CERT drive biogenesis of RNA-containing extracellular vesicles at ER membrane contact sites. *Dev Cell* **57**, 974-994 e978 (2022).
25. D. Rajgor *et al.*, Local miRNA-Dependent Translational Control of GABA(A)R Synthesis during Inhibitory Long-Term Potentiation. *Cell Rep* **31**, 107785 (2020).
26. P. Osten, L. Valsamis, A. Harris, T. C. Sacktor, Protein synthesis-dependent formation of protein kinase Mzeta in long-term potentiation. *J Neurosci* **16**, 2444-2451 (1996).
27. C. Glock *et al.*, The translatome of neuronal cell bodies, dendrites, and axons. *Proc Natl Acad Sci U S A* **118**, (2021).
28. Y. E. Wu, N. N. Parikshak, T. G. Belgard, D. H. Geschwind, Genome-wide, integrative analysis implicates microRNA dysregulation in autism spectrum disorder. *Nat Neurosci* **19**, 1463-1476 (2016).
29. M. Jin *et al.*, Establishment of a schizophrenia classifier based on peripheral blood signatures and investigation of pathogenic miRNA-mRNA regulation. *J Psychiatr Res* **159**, 172-184 (2023).
30. S. I. Kano, E. Dohi, I. V. L. Rose, Extracellular Vesicles for Research on Psychiatric Disorders. *Schizophr Bull* **45**, 7-16 (2019).
31. N. Vassileff, L. Cheng, A. F. Hill, Extracellular vesicles - propagators of neuropathology and sources of potential biomarkers and therapeutics for neurodegenerative diseases. *J Cell Sci* **133**, (2020).
32. S. S. Moy *et al.*, Sociability and preference for social novelty in five inbred strains: an approach to assess autistic-like behavior in mice. *Genes Brain Behav* **3**, 287-302 (2004).
33. E. Dohi *et al.*, Behavioral Changes in Mice Lacking Interleukin-33. *eNeuro* **4**, (2017).
34. M. Yang, J. N. Crawley, Simple behavioral assessment of mouse olfaction. *Curr Protoc Neurosci* **Chapter 8**, Unit 8 24 (2009).
35. M. Niwa *et al.*, Knockdown of DISC1 by in utero gene transfer disturbs postnatal dopaminergic maturation in the frontal cortex and leads to adult behavioral deficits. *Neuron* **65**, 480-489 (2010).
36. C. Thery *et al.*, Minimal information for studies of extracellular vesicles 2018 (MISEV2018): a position statement of the International Society for Extracellular Vesicles and update of the MISEV2014 guidelines. *J Extracell Vesicles* **7**, 1535750 (2018).

37. S. Sakamoto *et al.*, Alterations in circulating extracellular vesicles underlie social stress-induced behaviors in mice. *FEBS Open Bio* **11**, 2678-2692 (2021).
38. T. Arab *et al.*, Characterization of extracellular vesicles and synthetic nanoparticles with four orthogonal single-particle analysis platforms. *J Extracell Vesicles* **10**, e12079 (2021).
39. S. Kano *et al.*, The contribution of transcription factor IRF1 to the interferon-gamma-interleukin 12 signaling axis and TH1 versus TH-17 differentiation of CD4+ T cells. *Nat Immunol* **9**, 34-41 (2008).
40. S. Bariselli *et al.*, Role of VTA dopamine neurons and neuroligin 3 in sociability traits related to nonfamiliar conspecific interaction. *Nat Commun* **9**, 3173 (2018).
41. S. I. Kano *et al.*, Glutathione S-transferases promote proinflammatory astrocyte-microglia communication during brain inflammation. *Sci Signal* **12**, (2019).
42. J. Schindelin *et al.*, Fiji: an open-source platform for biological-image analysis. *Nat Methods* **9**, 676-682 (2012).
43. A. Dobin *et al.*, STAR: ultrafast universal RNA-seq aligner. *Bioinformatics* **29**, 15-21 (2013).
44. S. Anders, P. T. Pyl, W. Huber, HTSeq--a Python framework to work with high-throughput sequencing data. *Bioinformatics* **31**, 166-169 (2015).
45. M. I. Love, W. Huber, S. Anders, Moderated estimation of fold change and dispersion for RNA-seq data with DESeq2. *Genome Biol* **15**, 550 (2014).
46. Y. Zhou *et al.*, Metascape provides a biologist-oriented resource for the analysis of systems-level datasets. *Nat Commun* **10**, 1523 (2019).
47. A. Kozomara, S. Griffiths-Jones, miRBase: annotating high confidence microRNAs using deep sequencing data. *Nucleic Acids Res* **42**, D68-73 (2014).
48. R. G. Urdinguio *et al.*, Disrupted microRNA expression caused by Mecp2 loss in a mouse model of Rett syndrome. *Epigenetics* **5**, 656-663 (2010).
49. H. Wu *et al.*, Genome-wide analysis reveals methyl-CpG-binding protein 2-dependent regulation of microRNAs in a mouse model of Rett syndrome. *Proc Natl Acad Sci U S A* **107**, 18161-18166 (2010).
50. T. L. Cheng *et al.*, MeCP2 suppresses nuclear microRNA processing and dendritic growth by regulating the DGCR8/Drosha complex. *Dev Cell* **28**, 547-560 (2014).
51. Y. Gao *et al.*, Inhibition of miR-15a Promotes BDNF Expression and Rescues Dendritic Maturation Deficits in MeCP2-Deficient Neurons. *Stem Cells* **33**, 1618-1629 (2015).
52. D. Edbauer *et al.*, Regulation of synaptic structure and function by FMRP-associated microRNAs miR-125b and miR-132. *Neuron* **65**, 373-384 (2010).
53. X. L. Xu *et al.*, FXR1P but not FMRP regulates the levels of mammalian brain-specific microRNA-9 and microRNA-124. *J Neurosci* **31**, 13705-13709 (2011).
54. T. Liu *et al.*, A MicroRNA Profile in Fmr1 Knockout Mice Reveals MicroRNA Expression Alterations with Possible Roles in Fragile X Syndrome. *Mol Neurobiol* **51**, 1053-1063 (2015).
55. M. Zhang *et al.*, Identification of differentially expressed microRNAs and their target genes in the hippocampal tissues of Fmr1 knockout mice. *Am J Transl Res* **12**, 813-824 (2020).

56. Y. Hara *et al.*, Prenatal exposure to valproic acid increases miR-132 levels in the mouse embryonic brain. *Mol Autism* **8**, 33 (2017).
57. Y. Ozkul *et al.*, A heritable profile of six miRNAs in autistic patients and mouse models. *Sci Rep* **10**, 9011 (2020).
58. A. Kumari, P. Singh, M. S. Baghel, M. K. Thakur, Social isolation mediated anxiety like behavior is associated with enhanced expression and regulation of BDNF in the female mouse brain. *Physiol Behav* **158**, 34-42 (2016).
59. C. H. Chang, E. J. W. Kuek, C. L. Su, P. W. Gean, MicroRNA-206 Regulates Stress-Provoked Aggressive Behaviors in Post-weaning Social Isolation Mice. *Mol Ther Nucleic Acids* **20**, 812-822 (2020).
60. N. Popa, F. Boyer, F. Jaouen, R. Belzeaux, E. Gascon, Social Isolation and Enrichment Induce Unique miRNA Signatures in the Prefrontal Cortex and Behavioral Changes in Mice. *iScience* **23**, 101790 (2020).
61. S. Haramati *et al.*, MicroRNA as repressors of stress-induced anxiety: the case of amygdalar miR-34. *J Neurosci* **31**, 14191-14203 (2011).
62. C. Dias *et al.*, beta-catenin mediates stress resilience through Dicer1/microRNA regulation. *Nature* **516**, 51-55 (2014).
63. A. Torres-Berrio *et al.*, DCC Confers Susceptibility to Depression-like Behaviors in Humans and Mice and Is Regulated by miR-218. *Biol Psychiatry* **81**, 306-315 (2017).
64. N. Volk *et al.*, Amygdalar MicroRNA-15a Is Essential for Coping with Chronic Stress. *Cell Rep* **17**, 1882-1891 (2016).
65. Z. F. Deng *et al.*, miR-214-3p Targets beta-Catenin to Regulate Depressive-like Behaviors Induced by Chronic Social Defeat Stress in Mice. *Cereb Cortex* **29**, 1509-1519 (2019).
66. K. Du, W. Lu, Y. Sun, J. Feng, J. H. Wang, mRNA and miRNA profiles in the nucleus accumbens are related to fear memory and anxiety induced by physical or psychological stress. *J Psychiatr Res* **118**, 44-65 (2019).
67. N. Khandelwal, S. K. Dey, S. Chakravarty, A. Kumar, miR-30 Family miRNAs Mediate the Effect of Chronic Social Defeat Stress on Hippocampal Neurogenesis in Mouse Depression Model. *Front Mol Neurosci* **12**, 188 (2019).
68. A. Torres-Berrio *et al.*, miR-218 in Adolescence Predicts and Mediates Vulnerability to Stress. *Biol Psychiatry* **89**, 911-919 (2021).
69. Z. Miao *et al.*, Presence of the pregnant partner regulates microRNA-30a and BDNF levels and protects male mice from social defeat-induced abnormal behaviors. *Neuropharmacology* **159**, 107589 (2019).
70. M. L. Pfau *et al.*, Role of Monocyte-Derived MicroRNA106b approximately 25 in Resilience to Social Stress. *Biol Psychiatry* **86**, 474-482 (2019).
71. P. X. Luo *et al.*, Sex-specific effects of social defeat stress on miRNA expression in the anterior BNST. *Behav Brain Res* **401**, 113084 (2021).
72. Z. Miao *et al.*, Anxiety-Related Behaviours Associated with microRNA-206-3p and BDNF Expression in Pregnant Female Mice Following Psychological Social Stress. *Mol Neurobiol* **55**, 1097-1111 (2018).

73. T. Xu *et al.*, miRBaseConverter: an R/Bioconductor package for converting and retrieving miRNA name, accession, sequence and family information in different versions of miRBase. *BMC Bioinformatics* **19**, 514 (2018).

74. H. Y. Huang *et al.*, miRTarBase 2020: updates to the experimentally validated microRNA-target interaction database. *Nucleic Acids Res* **48**, D148-D154 (2020).

75. D. Santovito *et al.*, Plasma microRNA signature associated with retinopathy in patients with type 2 diabetes. *Sci Rep* **11**, 4136 (2021).